


Cite this: *RSC Adv.*, 2023, 13, 12844

# Crystal structure and optical characterization of a new hybrid compound, $C_6H_9N_2FeCl_4$ , with large dielectric constants for field-effect transistors†

A. Ghoudi,<sup>a</sup> Kh. Ben Brahim,<sup>a</sup> H. Ghalla,<sup>b</sup> J. Lhoste,<sup>c</sup> S. Auguste,<sup>c</sup> K. Khirouni,<sup>d</sup> A. Aydi<sup>a</sup> and A. Oueslati<sup>a</sup>

Due to remarkable dielectric features, such as a large dielectric constant, strong electrical conductivity, high capacitance, and low dielectric loss, hybrid materials have lately seen a huge number of applications in the field of optoelectronics. These are critical characteristics that qualify the performance of optoelectronic devices, particularly field-effect transistor components (FETs). Here, the hybrid compound 2-amino-5-picoline tetrachloroferrate(III) ( $2A5PFeCl_4$ ) was synthesised by using the slow evaporation solution growth method at room temperature. Structural, optical, and dielectric properties have been investigated. The  $2A5PFeCl_4$  compound crystallises in the monoclinic system ( $P2_1/c$  space group). Its structure can be described as a successive layering of inorganic and organic parts.  $[FeCl_4]^-$  tetrahedral anions and 2-amino-5-picolinium cations are connected by  $N-H\cdots Cl$  and  $C-H\cdots Cl$  hydrogen bonds. The optical absorption measurement confirms the semiconductor nature with a band gap of around 2.47 eV. Additionally, the structural and electronic properties of the title compound have been investigated theoretically through DFT calculations. At low frequencies, this material has significant dielectric constants ( $\epsilon \sim 10^6$ ). Furthermore, the high electrical conductivity, low dielectric loss at high frequencies, and high capacitance show that this new material has great dielectric potential in FET technologies. Due to their high permittivity, these compounds can be employed as gate dielectrics.

Received 23rd February 2023  
Accepted 18th April 2023

DOI: 10.1039/d3ra01239e

rsc.li/rsc-advances

## 1. Introduction

The field-effect transistor (FET) is usually considered the most important innovation of the twentieth century. Since the creation of the first silicon transistor in 1947, electronic technology has advanced dramatically.<sup>1–3</sup> It is a significant part of making contemporary digital integrated circuits. Silicon (Si)-based integrated circuits are employed in the majority of today's electronic products.<sup>4</sup> Actually, Moore's law states that by shrinking the constituent size of Si-based transistors, the dimensions of these integrated circuits can be reduced to improve their performance.<sup>5</sup>

Silicon has reached its fundamental limits as a material, notwithstanding its abundance and ease of handling.<sup>6</sup> However, one of its primary drawbacks is its inability to withstand the high temperatures created by current integrated circuits.<sup>7</sup> In this context, discovering new flexible materials with remarkable optical, dielectric, electrical, and mechanical characteristics is critical for the development of various electronic devices, particularly FETs.<sup>8</sup>

Due to the benefits of both organic and inorganic components, hybrid materials have drawn a lot of interest in optoelectronic devices such as light-emitting diodes (LEDs), solar cells, lasers, detectors, and photodetectors.<sup>9–16</sup> Aside from their widespread usage in photovoltaic applications, particularly solar cells, hybrids have lately piqued the interest of transistor researchers.<sup>15,16</sup> They are good candidates for FETs because of their low exciton binding energy, trap density, and other electric and dielectric properties, such as their high dielectric constant, good electrical conductivity, high capacitance, and low dielectric loss.

Recently, technology has been developed that takes advantage of hybrid materials' multifunctional capabilities in FET devices. They have been used in some works as dielectric gates in flexible thin-film transistors because of their high permittivity.<sup>17</sup> However, in other studies, these materials were used as

<sup>a</sup>Laboratory for Spectroscopic Characterization and Optics of Materials, Faculty of Sciences, University of Sfax, B. P. 1171, 3000 Sfax, Tunisia. E-mail: oueslatiabderrazek@yahoo.fr

<sup>b</sup>Quantum and Statistical Physics Laboratory, Faculty of Sciences, University of Monastir, Monastir 5079, Tunisia

<sup>c</sup>Institut des Molécules et Matériaux du Mans (IMMM), UMR-6283 CNRS, Le Mans Université, Avenue Olivier Messiaen, 72085 Le Mans Cedex 9, France

<sup>d</sup>Laboratoire de Physique des Matériaux et des Nanomatériaux appliquée à l'Environnement, Faculté des Sciences de Gabes, Université de Gabes, cite Erriadh, 6079 Gabes, Tunisia

† Electronic supplementary information (ESI) available. CCDC 2223635. For ESI and crystallographic data in CIF or other electronic format see DOI: <https://doi.org/10.1039/d3ra01239e>



active channels or semiconductors in creative transistor designs.<sup>18</sup>

Given the variety of crystal structures found in hybrid materials, we were able to successfully create a new hybrid compound, 2A5PFeCl<sub>4</sub>, using the slow evaporation solution growth method at room temperature. Its general formula is AMX<sub>4</sub> (where A stands for the organic cation, M for the inorganic cation, and X for the monovalent halogen ion (Cl<sup>−</sup>)).

The X-ray diffraction technique was used to characterize the title compound. The optical and dielectric properties have been determined. Further, DFT and TD-DFT calculations have been performed to determine the structure and electronic properties of 2A5PFeCl<sub>4</sub>. The absorption spectrum, wavelength, and HOMO–LUMO gap are calculated. The interactions between the organic and inorganic species, ensuring the stability of the crystal pattern, have been discussed through the Hirshfeld surfaces (HS), atoms in molecules (AIM), and non-covalent reduced density gradient (NC-RDG) analyses.

Due to the novelty of this hybrid material, a proper examination of its structural, optical, and electrical properties is required to ascertain whether it can be used in FET devices.

## 2. Experimental procedure

### 2.1. Crystallization of 2A5PFeCl<sub>4</sub>

The 2A5PFeCl<sub>4</sub> molecule was synthesised using a similar preparation procedure to other hybrid compounds that have been reported before (solvent evaporation method).<sup>19–21</sup>

An aqueous solution of ferric chloride was prepared by dissolving *ca.* 0.1 g of FeCl<sub>2</sub> in hydrochloric acid (HCl). To this solution, 0.0568 g of 2-amino-5-picoline (C<sub>6</sub>H<sub>8</sub>N<sub>2</sub>) was added. Single crystals, having a brown color, were obtained after 7 days.

### 2.2. Single crystal X-ray data collection

Crystals were selected under a polarizing optical microscope and mounted on micro mount needles (MiTiGen) for single-crystal X-ray diffraction experiments. X-ray intensity data were collected on a Bruker APEX II Quazar diffractometer (4 circle Kappa goniometer, CCD detector) using an I $\mu$ s microfocus source (Mo-K $\alpha$  radiation with  $\lambda = 0.71073$  Å) at 296 K. The structures were determined by direct methods with SHELXS-97 and SHELXL-97 programs included in the WINGX package.<sup>22</sup> All non-hydrogen atoms positions were refined anisotropically. Hydrogen atoms of the organic molecules were geometrically constrained (HFIX options). The nature of the atoms was differentiated from bond distance considerations. DIAMOND<sup>23</sup> was used to create the drawing. Crystallographic data for the structures have been deposited to the Cambridge Crystallographic Data Center, with the following number: CCDC 2223635† for C<sub>6</sub>H<sub>9</sub>N<sub>2</sub>FeCl<sub>4</sub>.

The structure refinement of the complex 2A5PFeCl<sub>4</sub> was performed in the monoclinic system with the  $P2_1/c$  space group (the point group 2/m). Lattice spacing are  $a = 6.4063(4)$  Å,  $b = 14.2730(9)$  Å,  $c = 13.2376(10)$  Å,  $\beta = 90.298(3)^\circ$  and  $V = 1210.4(2)$  Å<sup>3</sup> as listed in Table 1 along with data collection parameters and refinement. Selected experimental and calculated bond lengths and angles are listed in Table 3. It must be noted that the

**Table 1** Crystal and refinement data obtained for 2A5PFeCl<sub>4</sub> compound

Temperature	296 K
Empirical formula	C <sub>6</sub> H <sub>9</sub> N <sub>2</sub> FeCl <sub>4</sub>
Formula weight (g mol <sup>−1</sup> )	306.80
Crystal system	Monoclinic
Space group	$P2_1/c$
<i>a</i>	6.4063(4) Å
<i>b</i>	14.2730(9) Å
<i>c</i>	13.2376(10) Å
$\beta$	90.298(3)°
<i>Z</i>	4
<i>V</i>	1210.4(2) Å <sup>3</sup>
$\mu$ (Mo K $\alpha$ )	2.087 mm <sup>−1</sup>
Index ranges	$-8 < h < 8, -18 < k < 18, -17 < l < 16$
Reflections collected	16 901
Independent reflections	2783
Reflections with $I > 2\sigma(I)$	1710
$R_{\text{int}}$	0.041
Absorption correction	Multi-scan
Refined parameters	119
$R[F^2 > 2\sigma(F^2)]$	0.0320
$wR(F^2)$	0.1032
Goodness of fit	1.032
$\Delta\rho_{\text{min}}/\Delta\rho_{\text{max}}$ (Å <sup>−3</sup> )	−0.29/0.33

structure can be resolved in  $P2_1/m$  with  $c/2$ . Nevertheless, this solution has been excluded because it does not account for the order in the organic molecule in which nitrogen atoms are clearly localized.

### 2.3. Spectroscopic measurements

A Shimadzu UV-3101PC scanning spectrophotometer with a wavelength range of 200 to 800 nm was used to carry out UV-vis powder spectroscopy at room temperature. The apparatus has the capability of measuring absorbance and reflection with spherical integration and xenon light.

We used a Solartron impedance analyzer to investigate electrical transmission characteristics, operating within a frequency range of  $10^2$  to  $10^7$  Hz, at temperatures between 313 and 358 K and a voltage of 0.5 V. The measurements were carried out on a pellet with a typical diameter of 8 mm and a thickness 1 mm. The opposite sides of this pellet have been covered with conductive silver paint to ensure a solid electrical connection.

## 3. Theoretical details

Starting from its crystalline asymmetric unit, the geometry of 2A5PFeCl<sub>4</sub> was optimized with the DFT method. The optimization was carried out using the Gaussian 09 software package<sup>24</sup> and GaussView as an interface program.<sup>25</sup> The exchange functional (B3) of the Becke three-parameter hybrid<sup>26</sup> combined with the LYP functional (Lee–Yang–Parr correlation)<sup>27</sup> was employed in conjunction with the empirical dispersion corrections of Grimme D3,<sup>28</sup> and the LanL2DZ basis set.<sup>29</sup> The intermolecular interactions between organic and inorganic entities have been discussed through Hirshfeld surfaces, AIM and non-covalent



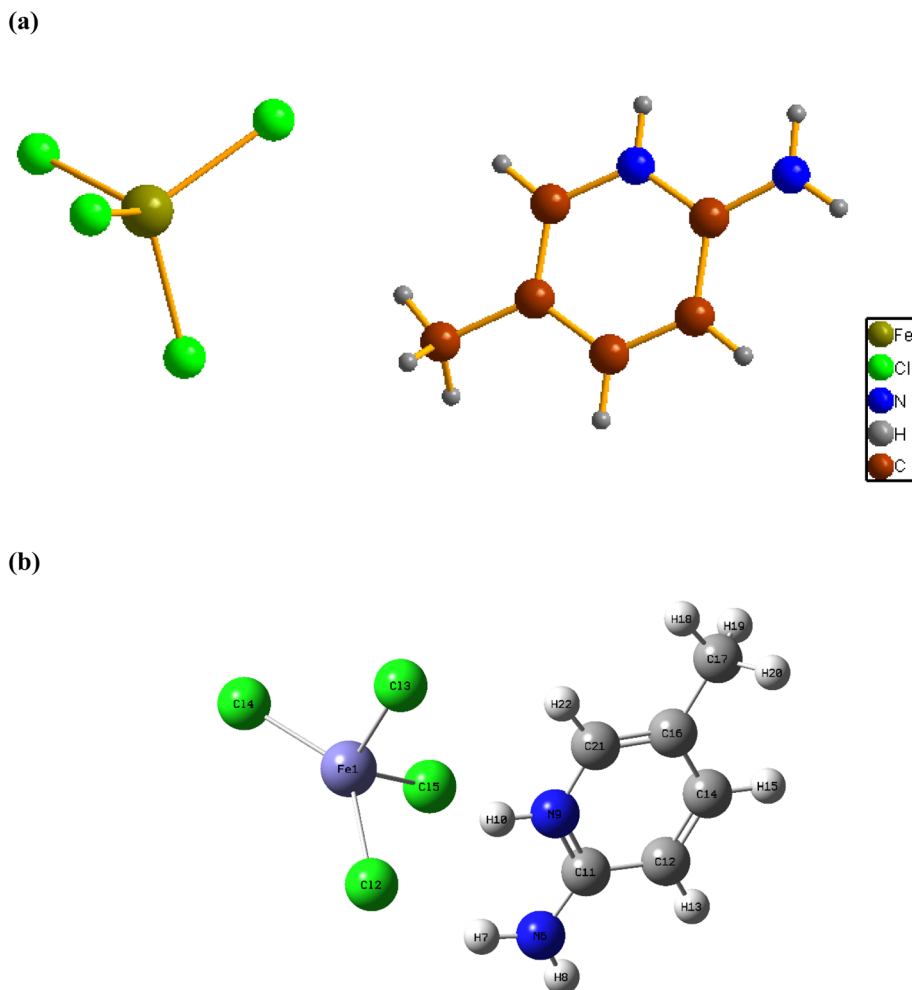


Fig. 1 Experimental (a) and optimized (b) geometries of 2A5PFeCl<sub>4</sub> compound.

RDG analyses. The Hirshfeld surfaces and fingerprint plots<sup>30</sup> were determined by using the Crystal Explorer package<sup>31</sup> based on the CIF file of the title compound. The topological AIM and RDG analyses have been performed with the Multiwfn program,<sup>32</sup> using the wavefunction file created through DFT single point calculation. The electrostatic potential surface was computed to identify the nucleophile and the electrophile sites. Further, TD-DFT calculations have been performed in order to predict the UV-vis absorption spectrum and to calculate the HOMO–LUMO energy gap employing the IEFPCM solvation model.

## 4. Results and discussion

### 4.1. Crystal structure description

Fig. 1a shows the asymmetric unit of 2A5PFeCl<sub>4</sub>, which is made up of a crystallographically independent [C<sub>6</sub>H<sub>9</sub>N<sub>2</sub>]<sup>+</sup> cation and an ion tetrachloroferrate(III). This finding fits well with the optimized geometry, calculated at the DFT/B3LYP-D3/LanL2DZ level of theory, as depicted in Fig. 1b.

To describe the atomic arrangement and better understand the crystalline architecture of the title molecule. Fig. 2 illustrates the projection along the  $\vec{c}$  axis.

Indeed, this projection demonstrates the atomic organization of chemical buildings involved in the composition of the crystal in the form of an alternation of cationic and anionic groups parallel to the (001) plane.

Based on the X-ray determination, the crystalline structure is mainly stabilized by the presence of two strong interactions N1–H1A...Cl<sub>4</sub>, N1–H1B...Cl<sub>1</sub>, since the values  $d(\text{H} \cdots \text{Cl})$  are smaller than the sum of the radii of van der Waals of the iron, and hydrogen atoms ( $r_{\text{Fe}} + r_{\text{H}} \leq 2.81 \text{ \AA}$ ),<sup>33</sup> and weak N/C–H...Cl hydrogen bonding. These interactions exhibit donor–acceptor distances ranging from 3.441 to 3.775 Å between the cationic and anionic entities, as can be seen in Table 2.

The [FeCl<sub>4</sub>]<sup>2–</sup> anion adopts a tetrahedral geometry in which the Fe ion is surrounded by four chlorine atoms with an sp<sup>3</sup> hybridization. The bond length Fe–Cl and bond angle Cl–Fe–Cl values are in the range of 2.1864(8)–2.2039(9) Å and 107.38(3)–111.68(4)°, respectively (Table 3).

On the other hand, we propose a very simple geometry index for four-coordinate transition metal complexes,  $\tau_4$ , given by the following eqn (1) by subtracting  $\alpha$  and  $\beta$ , the two largest angles in the tetra-coordinate species, from 360°, then dividing everything by 141.<sup>34</sup>



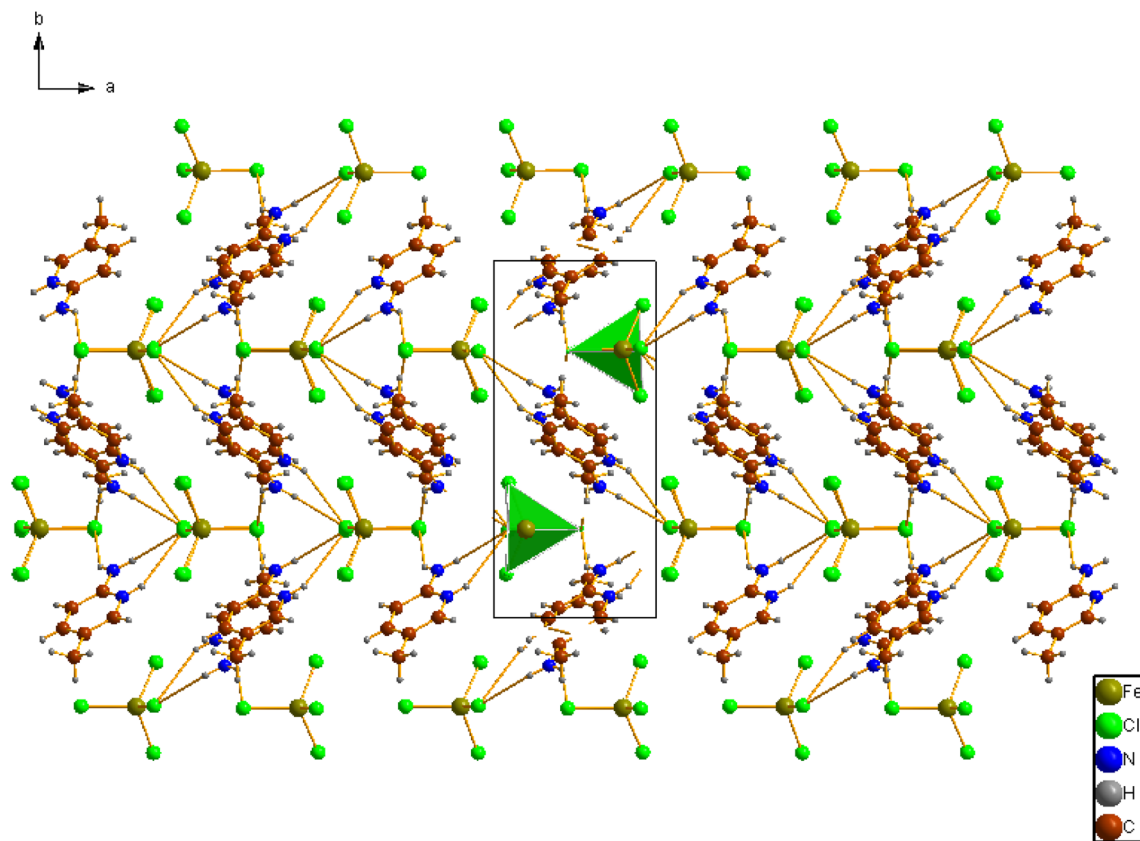


Fig. 2 Projection along the *c* axis of the atomic arrangement of 2A5PFeCl<sub>4</sub>.

Table 2 Hydrogen-bond parameters (bond length in Å, bond angle in degrees)

D–H⋯A	D–H	H⋯A	D⋯A	D–H⋯A
N1–H1A⋯Cl3	0.86	2.976	3.474	118.8
N1–H1A⋯Cl4	0.86	2.785	3.568	152.0
N1–H1B⋯Cl1	0.86	2.721	3.441	142.2
N2–H2⋯Cl4	0.86	2.853	3.631	151.4
C2–H2A⋯Cl3	0.93	2.884	3.775	160.7
C6–H6⋯Cl2	0.93	2.924	3.560	126.8

$$\tau_4 = \frac{360^\circ - (\alpha + \beta)}{141^\circ} \quad (1)$$

The tetra-coordinate  $\tau_4$  index is found to be 0.98. A tetra-coordinate index is a number that ranges from 0.0 for a perfect square planar geometry to 1.0 for a perfect tetrahedral geometry. Interestingly, this agrees with the X-ray results, as  $\tau_4$  is very close to the unit, which is almost a perfect tetrahedron.

The Baur distortion indices for the distances and angles can be calculated using eqn (2) and (3):<sup>35</sup> where  $d = (\text{Fe–Cl})$  distance,  $a = (\text{Cl–Fe–Cl})$  angle, and  $d_m = \text{average value}$ .

$$\text{ID}(\text{Fe–Cl}) = \sum_{i=1}^{n_1} \frac{|d_i - d_m|}{4 d_m} \quad (2)$$

$$\text{ID}(\text{Fe–Cl–Cl}) = \sum_{i=1}^{n_2} \frac{|a_i - a_m|}{6 a_m} \quad (3)$$

$$\text{ID}(\text{Fe–Cl}) = 3.05(1) \times 10^{(-3)} \text{ and } \text{ID}(\text{Cl–Fe–Cl}) = 0.010 (8).$$

It can be admitted that the FeCl<sub>4</sub> tetrahedron is formed by a regular arrangement of chlorine atoms, in which the iron atom is slightly displaced from the center of gravity of the tetrahedron.

Concerning the cationic group, the latter has a plane geometry, a pyridine group coplanar with the methyl (–CH<sub>3</sub>) on the C5 atom with a C4–C5 distance equal to 1.503(4) Å and an amino group with a distance C1–N1 = 1.339(4) Å.

The pyridine group is characterized by C–C and C–N bond lengths ranging from 1.334(4) to 1.399(4) Å and bond angles, C–C–C, C–N–C and C–C–N varying from 116.8(4) to 123.2(3)° (Table 3). These values are comparable to the corresponding ones previously reported for similar pyridinium complexes.<sup>36</sup>

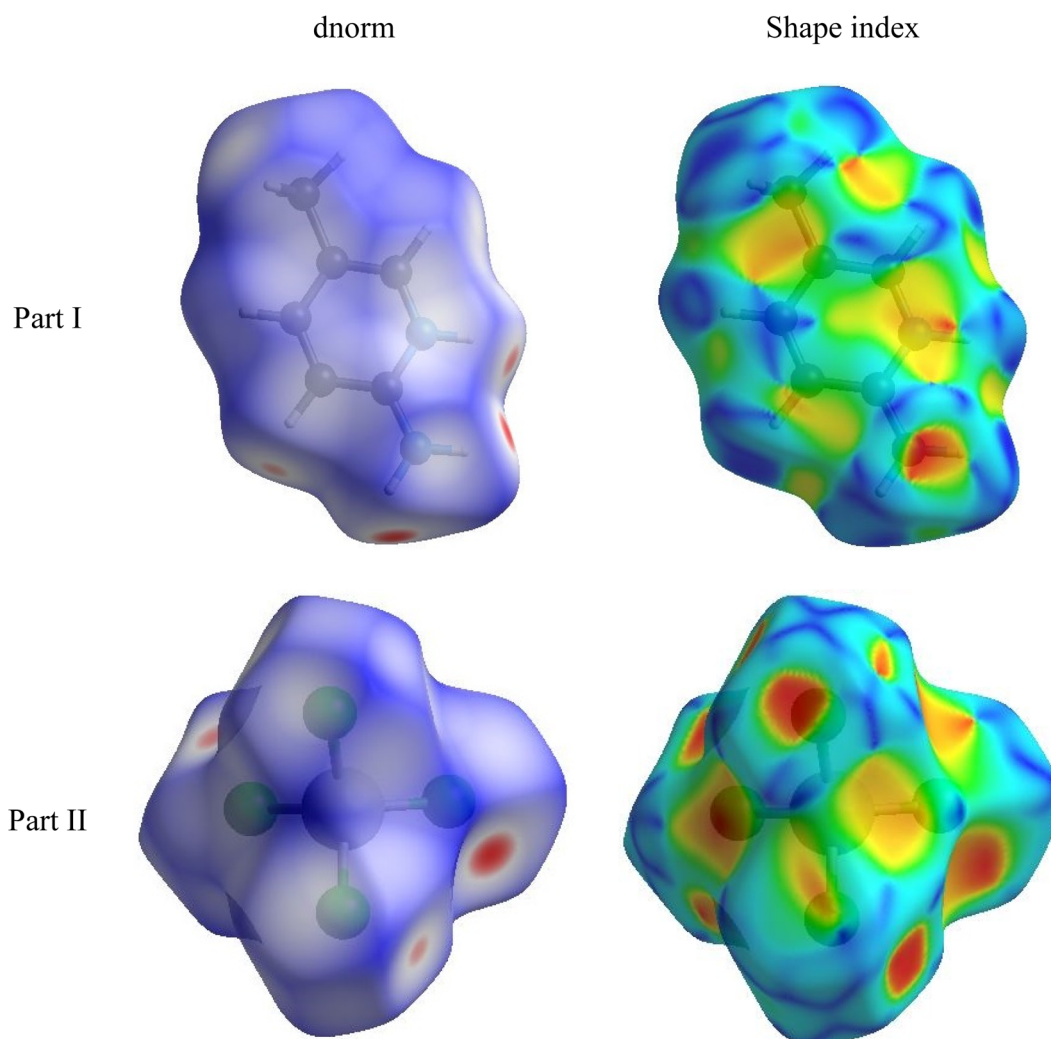
#### 4.2. Hirshfeld surfaces

The Hirshfeld surfaces generated from the crystal packing give a significant interpretation of the possible interactions ensuring the stability of the crystal.<sup>36</sup> The basic goal of the Hirshfeld surface is to divide the crystal electron density into molecular fragments by defining the area occupied by a molecule in a crystal. In this context, two alternative types of



Table 3 Geometrical parameters of 2A5PFeCl<sub>4</sub> obtained by DFT calculations and experimental XRD measurements

Bond lengths (Å)	Observed	Calculated	Angle (°)	Observed	Calculated
<b>[FeCl<sub>4</sub>]<sup>−</sup></b>					
Fe1–Cl1	2.1864(8)	2.295	Cl1–Fe1–Cl2	109.46(3)	98
Fe1–Cl2	2.1921(8)	2.241	Cl1–Fe1–Cl3	107.38(3)	136
Fe1–Cl3	2.2014(8)	2.198	Cl2–Fe1–Cl3	111.68(4)	103
Fe1–Cl4	2.2039(9)	2.238	Cl1–Fe1–Cl4	110.54(4)	100
			Cl2–Fe1–Cl4	108.00(5)	112
			Cl3–Fe1–Cl4	109.81(4)	107
<b>[C<sub>6</sub>H<sub>9</sub>N<sub>2</sub>]<sup>+</sup></b>					
N1–C1	1.339(4)	1.354	C1–N2–C6	123.2(3)	124
N2–C1	1.334(4)	1.368	N2–C1–N1	119.7(3)	119
N2–C6	1.355(4)	1.375	N2–C1–C2	116.8(3)	117
C1–C2	1.399(4)	1.427	N1–C1–C2	123.5(3)	124
C2–C3	1.351(4)	1.387	C3–C2–C1	119.8(3)	120
C3–C4	1.380(4)	1.30	C2–C3–C4	122.1(3)	122
C4–C6	1.347(4)	1.384	C6–C4–C3	116.9(3)	117
C4–C5	1.503(4)	1.512	C6–C4–C5	121.5(3)	122
			C3–C4–C5	121.6(3)	122

Fig. 3 Graphical plots of Hirshfeld surfaces mapped with  $d_{\text{norm}}$  and shape index.



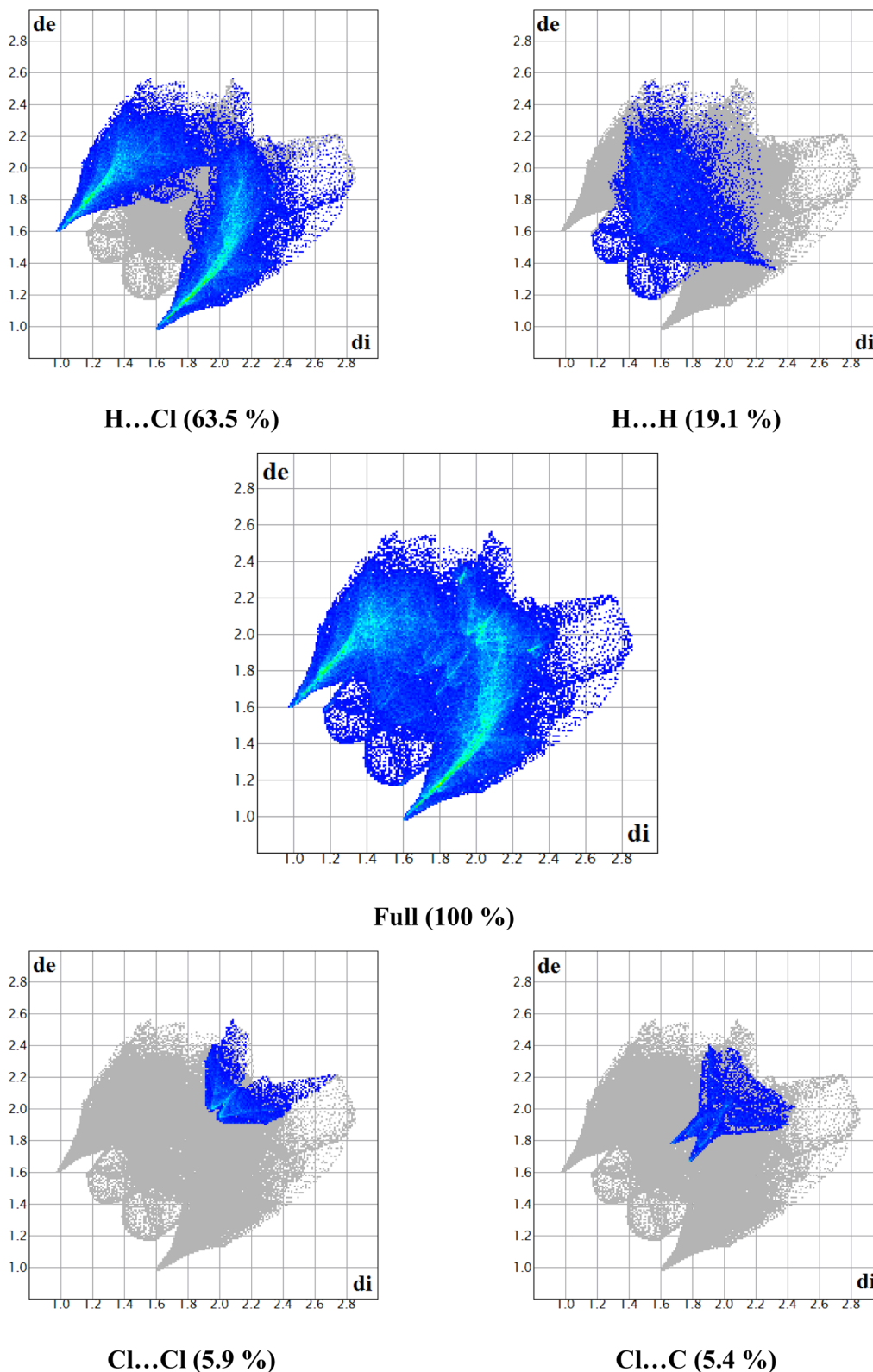


Fig. 4 2D-fingerprint plots along with the percentage of main intermolecular contacts contributed to the Hirshfeld surface in 2-amino 5-picoline tetrachloroferrate(III) crystal packing.

distances  $d_e$  and  $d_i$  are specified for each point of an isosurface, expressing the distance from the point to the closest nucleus either external to the surface or internal to the surface,

respectively. The normalized contact distance  $d_{\text{norm}}$  was used to define a three-dimensional molecular surface.  $d_{\text{norm}}$  is characterized by:<sup>37</sup>

$$d_{\text{norm}} = \frac{d_i - r_i^{\text{vdW}}}{r_i^{\text{vdW}}} + \frac{d_e - r_e^{\text{vdW}}}{r_e^{\text{vdW}}} \quad (4)$$

where  $r_e^{\text{vdW}}$  and  $r_i^{\text{vdW}}$  are the van der Waals (vdW) radii of the two atoms external and internal to the Hirshfeld surface, respectively. Fig. 3 shows the Hirshfeld surfaces of 2A5PF<sub>4</sub>Cl<sub>4</sub>, mapped using  $d_{\text{norm}}$  and shape index representations. The intermolecular interactions are plotted using a color code; the contacts that have distances equal to the sum of the vdW radii are depicted in white, while those that have distances that are less than or more than the vdW radii are displayed in red and blue, respectively. The red spots on the  $d_{\text{norm}}$  mapped Hirshfeld surface indicate the presence of intermolecular H-bonds. As shown with dotted lines, the dark-red spots on the DNRM surface indicate short interatomic contacts, *i.e.*, the strong hydrogen bonds N–H $\cdots$ N C–H $\cdots$ Cl, and N–H $\cdots$ Cl donor–acceptor.

The Hirshfeld surface can alter very subtly and have a significant impact on the shape index. The latter shows the surface of electron density that surrounds molecular interactions. The small range of light color represents a weaker and longer interaction than hydrogen bonds. Red and blue triangles are a sign of  $\pi$ – $\pi$  interactions. The griddle-colored regions in each of di and de represent all intra- and intermolecular interactions in the 2D fingerprint plots, as shown in Fig. 4. Accordingly, the main interaction contributions to the whole Hirshfeld surface are H $\cdots$ Cl (63.5%) H $\cdots$ H (19.1%), Cl $\cdots$ Cl (5.9%) and Cl $\cdots$ C (5.4%) contacts. So, this quantitative finding demonstrates that H $\cdots$ Cl interactions account for the majority of the surface.

### 4.3. AIM analysis

Within AIM theory,<sup>38</sup> each interatomic interaction is defined by the presence of a bond critical point (BCP). The topological parameters at BCP, such as the electron density  $\rho(r)$  and its Laplacian  $\Delta^2\rho(r)$ , aid in understanding the nature and strength

**Table 4** AIM topological parameters describing the organic–inorganic interactions in 2-amino 5-picoline tetrachloroferrate(III)<sup>a</sup>

BCP	$\rho(r)$	$\Delta^2\rho(r)$	$H(r)$	$G(r)$	$V(r)$	$E(r)$	$\epsilon$	ELF
1	0.0095	0.0326	0.0014	0.0068	−0.0054	7.03	0.1635	0.0318
2	0.0085	0.0291	0.0011	0.0062	−0.0051	6.61	3.1864	0.0267
3	0.0070	0.0230	0.0009	0.0048	−0.0039	5.07	0.7246	0.0227
4	0.0177	0.0502	0.0003	0.0122	−0.0119	15.53	0.0770	0.0741
5	0.0065	0.0208	0.0008	0.0044	−0.0036	4.70	0.5412	0.0210
6	0.0190	0.0548	0.0003	0.0134	−0.0131	17.04	0.0532	0.0771

<sup>a</sup> All parameters are given in au, except  $E(r)$  is expressed in kJ mol<sup>−1</sup>.

of the interaction.<sup>39</sup> According to Koch and Popelier criteria,<sup>40</sup> the hydrogen bonding interaction should have  $\rho(r)$  and  $\Delta^2\rho(r)$  values within the range of 0.0020–0.0400 and 0.0240–0.1390 a.u., respectively.

The molecular graph including BCPs associated with the intermolecular interactions between organic and inorganic entities in the asymmetric unit are displayed in Fig. 5. All of the topological parameters measured at the BCPs are listed in Table 4. When the value of  $\Delta^2\rho(r)$  at BCP is positive, it means that the electron density is being reduced along with the bond path, which is typical of closed-shell interactions like hydrogen

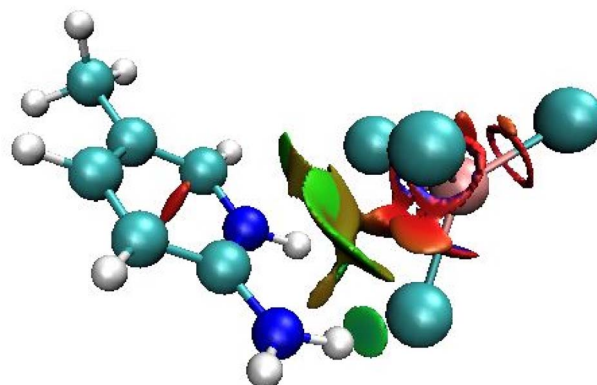


**Fig. 6** RDG function isosurface with  $\text{sign}(\lambda_2)\rho$  coloring scheme for the asymmetric unit cell of 2-amino 5-picoline tetrachloroferrate(II).

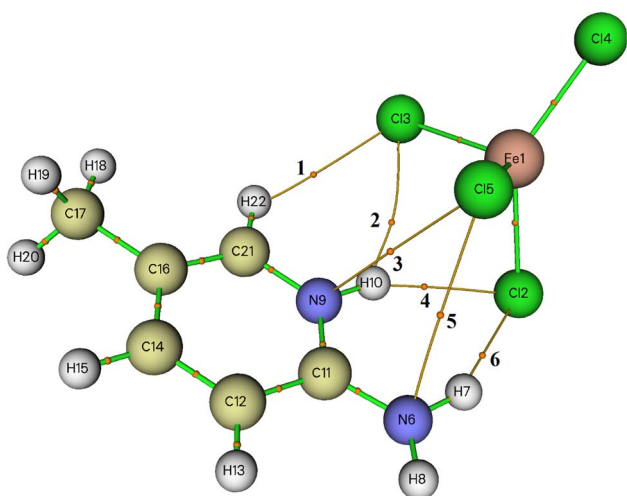


**Fig. 5** AIM molecular graph of 2-amino 5-picoline tetrachloroferrate(II) generated by using Multiwfn program: bond critical points (BCPs) are represented with small orange spheres.

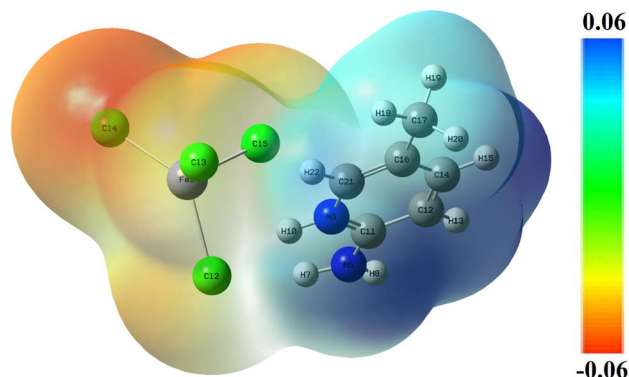


**Fig. 7** Molecular electrostatic potential surface of 2-amino 5-picoline tetrachloroferrate(II) calculated at B3LYP-D3/lanl2dz level of theory.



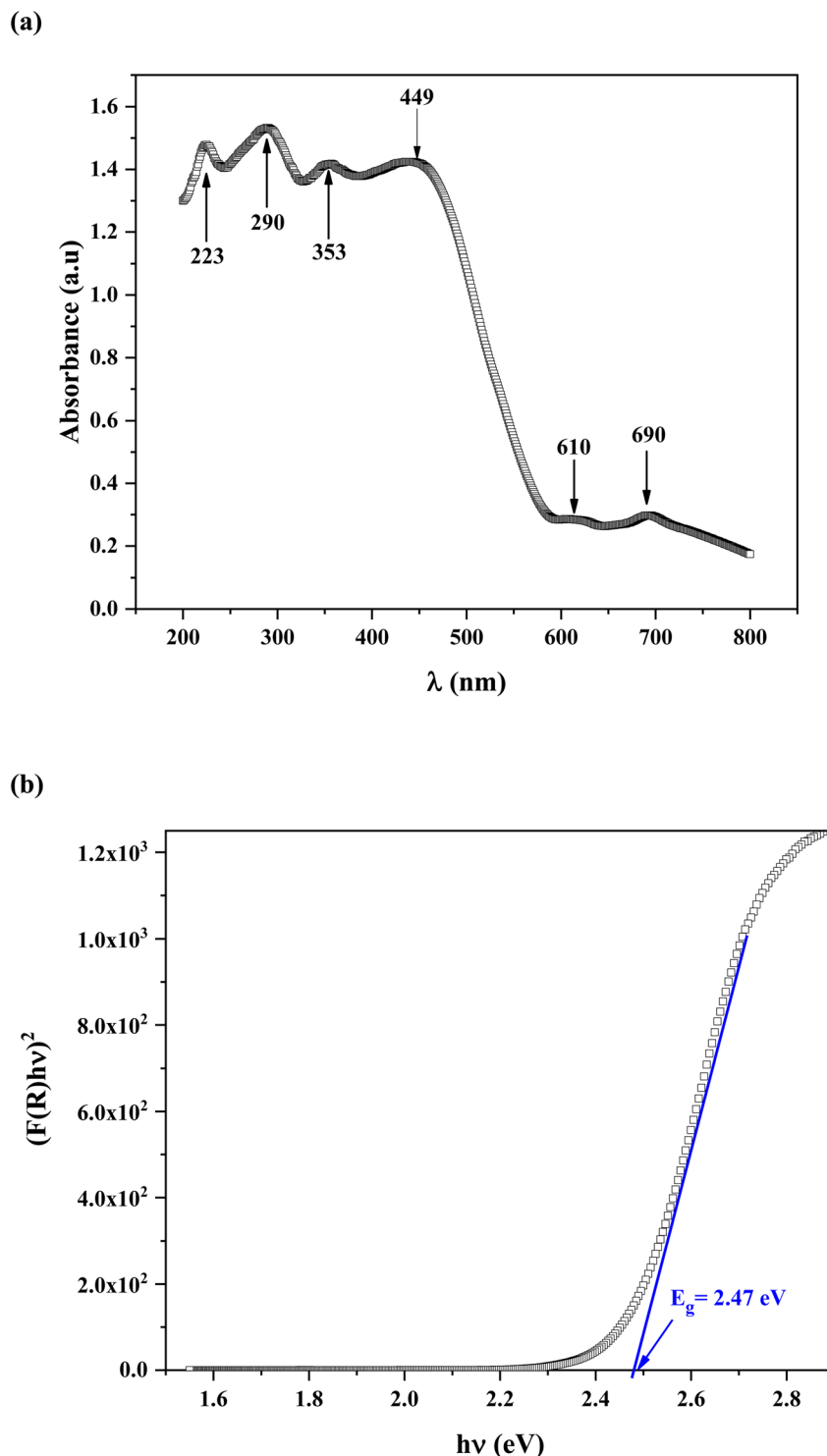


Fig. 8 (a) UV-vis absorption of 2A5PFeCl<sub>4</sub> compound and Tauc plot of 2A5PFeCl<sub>4</sub> (b) compound.

bonding. Here, the values of  $\rho(r)$  and  $\Delta^2\rho(r)$  are between 0.0065 and 0.0190 and 0.0208 and 0.0548, respectively. Regarding these parameters, we may conclude that the interactions between the organic and inorganic species are considerably weak; the values of  $\Delta^2\rho(r)$  are lower than those of Koch and Popelier criteria.

In order to discuss deeply the nature of the intermolecular interactions within the asymmetric unit, NCI-RDG analysis was performed.

This technique allows graphically distinguishing, with color coding, between hydrogen bonding, van der Waals, and repulsive steric interactions. The RDG function isosurface with



sign( $\lambda_2$ ) $\rho$  coloring scheme for the asymmetric unit cell of 2A5PFeCl<sub>4</sub> is depicted in Fig. 6. The green areas between the organic and inorganic parts prove the existence of van der Waals interactions.

#### 4.4. Molecular electrostatic potential

The surface of the molecular electrostatic potential (MEP) is related to the electronic density and is a useful descriptor for defining sites for electrophilic attack, nucleophilic reactions, and hydrogen-bonding interactions.<sup>41–43</sup> The calculated MEP surface of 2A5PFeCl<sub>4</sub> is plotted, using a color code, in Fig. 7. The nucleophilic sites are associated with the blue zone with positive potential, whereas the red region defines the electrophilic sites. An area with zero potential is shown by the color green. Herein, the nucleophilic attacks are located surrounding the hydrogen and nitrogen atoms of the organic part, while the electrophilic sites are associated with the inorganic part of the asymmetric unit. These findings reflect the interactions between the two parts of the compound and support the stability of the pattern.

#### 4.5. Optical absorption of 2A5PFeCl<sub>4</sub>

The semi-conductive properties of 2A5PFeCl<sub>4</sub> were explored using UV-vis spectroscopic analysis.

Fig. 8a present the experimental absorption spectrum. Six peaks are observed. The absorption bands are indicative of the electronic transitions within the inorganic component ([FeCl<sub>4</sub>]<sup>−</sup> anion), rather than the cation group, because organic molecules are transparent in the visible spectrum region.<sup>44</sup> The [FeCl<sub>4</sub>]<sup>−</sup> anion is typically ascribed to the four distinctive bands at 223, 290, 353 and 449 nm.<sup>45,46</sup> The other bands observed at 610 and 690 nm, assigned to <sup>4</sup>E(b) (<sup>6</sup>A<sub>1</sub> → <sup>4</sup>T<sub>2</sub>(b)) and <sup>6</sup>A<sub>1</sub> → <sup>4</sup>A<sub>2</sub> transitions respectively, are characteristic of the [FeCl<sub>4</sub>]<sup>−</sup> anion in a tetrahedral geometry.<sup>47</sup>

In addition, strong absorption is observed in the spectral region roughly between 200 and 450 nm then it decreases sharply from 450 to 600 nm, thus indicating the presence of the band gap.

The shoulders that emerge in the reflectance spectrum R occur at wavelengths corresponding to the optical gap, according to R. E. Marotti *et al.*<sup>48</sup> and R. Henriquez *et al.*<sup>49</sup> calculating the first derivative (1/R)(dR/dλ) highlights the shoulders. Fig. S1† depicts the first derivative variation as a function of wavelength. The existence of a prominent peak centred at 506 nm allows one to estimate the energy of the optical gap at 2.45 eV using the relationship:

$$E_g(\text{eV}) = \frac{1240}{\lambda \text{ (nm)}} \quad (5)$$

The band gap energy of C<sub>6</sub>H<sub>9</sub>N<sub>2</sub>FeCl<sub>4</sub> is also determined by combining both the Kubelka–Munk function and the Tauc equation, as shown by the following relation:<sup>50</sup>

$$F(R)h\nu = \frac{B}{S}(h\nu - E_g)^n \quad (6)$$

$F(R) = (1 - R)^2/2R$ , where  $R$  represents reflectance,  $\nu$  is the light frequency,  $h$  is Planck constant,  $B$  is a constant related to transition probability, and  $n$  is the index, which takes different values depending on the inter-band transition mechanism ( $n = 1/2$  and 2 corresponding to direct and indirect transitions, respectively).

Fig. 8b depicts the  $(F(R)h\nu)^2$  vs. photon energy ( $h\nu$ ) curve. The extension of the linear portion of the curve to meet the ( $h\nu$ ) axis at  $(F(R)h\nu)^2$  yields an optical band gap  $E_g = 2.47$  eV. This value is quite similar to that produced using the Marotti method. This value proves that the title compound is a suitable semiconductor for optoelectronics applications.<sup>51</sup>

The excitation characteristics and capability of electron transport may be reasonably predicted qualitatively using the border molecular orbital.<sup>52</sup>

Fig. 9 illustrates the superposition of the experimental and predicted UV-vis spectra. The TD-DFT spectra are computed in the gas phase and in water and HCl solvents using the IEFPCM solvation model. Clearly, the simulation spectra fairly fit the experimental absorption band of the investigated compound. One may observe that the simulated spectrum in water solvent reproduces the experimental one rather than in the gas phase and HCl solvent.

The most significant orbitals in a molecular system are the frontier molecular orbitals, called the highest occupied molecular orbital (HOMO) and the lowest unoccupied molecular orbital (LUMO). The frontier orbital gap characterizes the chemical reactivity and kinetic stability of the molecule. In this context, a molecule with a small frontier orbital gap is more polarizable. It is generally associated with a high chemical reactivity, and low kinetic stability and is also termed a soft molecule.<sup>52–54</sup> The HOMO is the orbital that primarily acts as an electron donor and the LUMO is the orbital that largely acts as an electron acceptor. HOMO−2, HOMO−1, HOMO, LUMO, LUMO+1 and LUMO+2 molecular orbital isosurfaces along with their energy values are illustrated in Fig. 10. The HOMO–LUMO

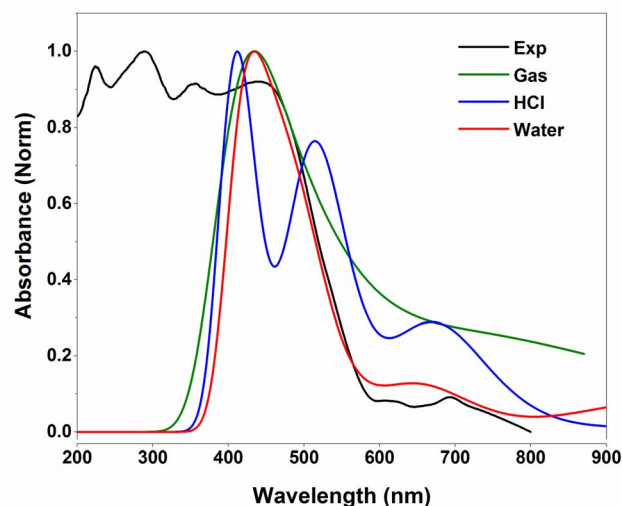


Fig. 9 Experimental and TD-DFT/B3LYP-D3 predicted UV-vis spectra of 2-amino-5-picoline tetrachloroferrate(III).



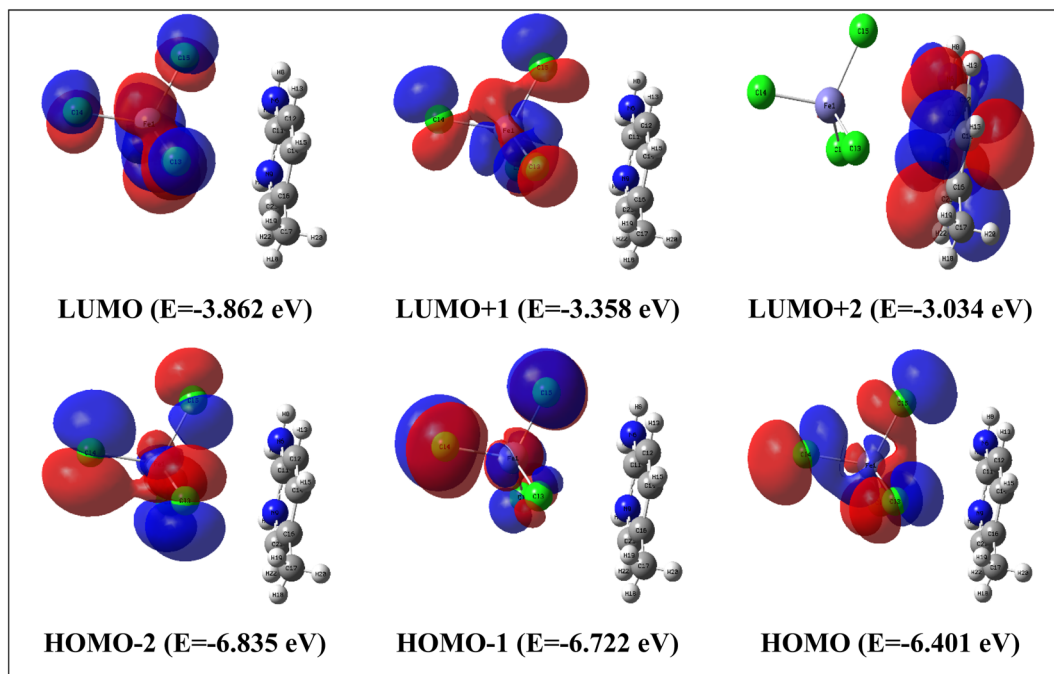


Fig. 10 HOMO and LUMO frontier molecular orbitals calculated with TD/B3LYP-D3/lanl2dz in water solvent.

energy gap is found to be 2.54 eV. This value explains the eventual charge transfer interactions within the molecules. The LUMO+2 isosurface is localized in the organic part. The other isosurfaces, HOMO-2, HOMO-1, HOMO, LUMO and LUMO+1, only occur on the inorganic part. To better understand the reactivity of the title compound, several energetic descriptors have been calculated based on the HOMO and LUMO energy values, such as chemical potential ( $\mu$ ), electronegativity ( $\chi$ ), global hardness ( $\eta$ ), global softness ( $\zeta$ ), and global electrophilicity index ( $\omega$ ) values. The results are listed in Table 5. The high electrophilicity index categorizes the propensity of electron acceptors to acquire additional electron charges from the environment. According to the literature,<sup>55</sup> the chemical in the title can provide semi-conducting characteristics.

**Table 5** TD-DFT calculations of HOMO–LUMO energy gap, chemical potential, electronegativity, global hardness, global softness, and electrophilicity index

Function	Value
$E_{\text{HOMO}}$ (eV)	−6.401
$E_{\text{LUMO}}$ (eV)	−3.862
$\Delta E_{\text{HOMO-LUMO}}$ gap (eV)	2.539
Chemical potential $\mu$ (eV)	−5.131
Electronegativity $\chi$ (eV)	5.131
Global hardness $\eta$ (eV)	1.269
Global softness $S$ (eV)	0.788
Global electrophilicity index $\psi$ (eV)	13.17
Dipole moment (D)	17.78
Counterpoise corrected energy (a.u.)	−526.893184234950
BSSE energy (a.u.)	0.004289900801
Complexation energy (kcal mol <sup>−1</sup> )	−121.27

#### 4.6. Dielectric measurements

Complex impedance spectroscopy (CIS) is a well-established technique for analysing a material's electrical activity. It provides information on ion flow inside the material, relaxation time, electrical conductivity, *etc.*

The polarizability of dielectric material is governed by its relative permittivity ( $\epsilon_r$ ) or dielectric constant ( $\epsilon$ ), which is commonly stated as a complex number given by:<sup>56</sup>

$$\epsilon = \epsilon' - i\epsilon'' \quad (7)$$

where the real part  $\epsilon'$  describes the power of the dipole configuration in the dielectric region and is defined as a measure of the energy accumulated in the matter from the electrical field applied. Whereas the imaginary part  $\epsilon''$  is thought to be the energy dissipated in the dielectric due to frictional damping, which prevents connected charge displacements from remaining in phase with field changes. The real and imaginary dielectric constants have been calculated using the following formula, based on  $Z'$  and  $Z''$  observations, respectively:

$$\epsilon' = \frac{Z''}{2\pi f C_0 (Z'^2 + Z''^2)} \quad (8)$$

$$\epsilon'' = \frac{Z'}{2\pi f C_0 (Z'^2 + Z''^2)} \quad (9)$$

where  $C_0$  represents the free space capacitance ( $C_0 = \epsilon_0 A/d$ , where  $A$  is the area and  $d$  is the pellet thickness),  $f$  stands for the frequency, and  $Z'$  and  $Z''$  are the real and imaginary parts of the impedance, respectively.



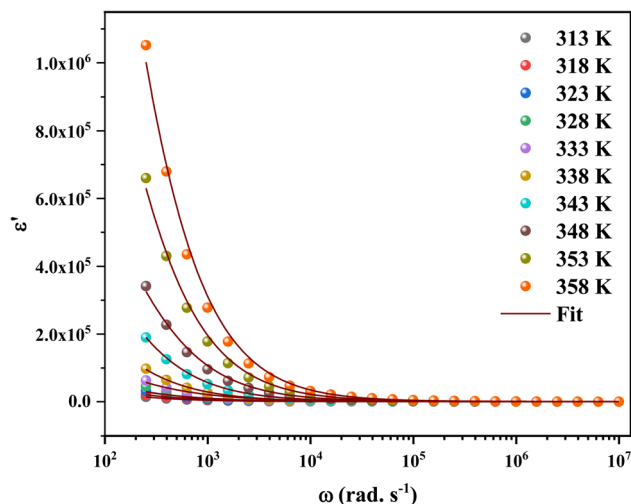


Fig. 11 Frequency-dependent real part of dielectric constants of 2A5PFeCl<sub>4</sub>.

The calculated frequency-dependent  $\epsilon'$  values at different temperatures are shown in Fig. 11. At low frequencies, the produced materials had greater  $\epsilon'$  values, indicating that they might be good candidates for low-frequency energy storage.<sup>57</sup> Similarly, the  $\epsilon'$  values fall as the frequency rises, improving the energy storage capacity.<sup>58</sup> Furthermore, the dielectric constant values rise as the temperature increases at a certain frequency. This nature specifies the thermal activation of charge carriers, which impacts polarization. The four main types of polarization are ionic, electronic, orientational, and interfacial. The system's ionic and electronic polarizations are deformational components of polarizability, whereas the orientational and interfacial polarizations are relaxation components.<sup>59</sup>

The Maxwell-Wagner interfacial polarization can explain the observed dielectric behavior in this material.<sup>60</sup> According to these models, the produced sample's dielectric structure is made up of good-conductive grains separated by poor-conductive grain boundaries. The grain boundaries act as a barrier, preventing charge carriers from flowing freely and lowering the inter-grain conductivity. Interfacial polarization involves electron exchange between the ions of the same molecule. Material deformation causes the distribution of positive and negative space charges to change. When an electric field is applied, negative and positive charges travel to opposing poles, resulting in a huge number of dipoles when the frequency is low. As a result, the dipoles easily follow the quasi-static field, and the material exhibits a high dielectric constant at low frequencies. As the dipole moments become incapable of following the electric field at higher frequencies, the dielectric constants steadily fall into the high-frequency zone.

The orientational and interfacial polarizations contribute to the real part of the dielectric constant in the low-frequency zone. On the other hand, the electronic and ionic polarizations are governed in the high frequency domain, which explains the lower values of  $\epsilon'$ . The existence of thermally activated charge carriers and the moment of the electric dipole are

responsible for the increase in the real component of the dielectric constant with increasing temperature.<sup>61,62</sup>

Based on the literature, the dielectric constants of some conventional semiconductors were substantially lower than those of C<sub>6</sub>H<sub>9</sub>N<sub>2</sub>FeCl<sub>4</sub> ( $\epsilon \sim 10^6$ ). For example, silicon<sup>63</sup> has a dielectric constant of 12.1 while organic semiconductors have dielectric constants ranging from 2 to 5, causing recombination losses in solar systems (photovoltaic devices).<sup>64–66</sup> On the other hand, materials with a high dielectric constant demonstrated more resistance to the electric field than those with low values.<sup>64</sup>

Furthermore, a large dielectric constant would reduce exciton binding energy, lowering charge carrier recombination losses, and thereby boosting solar cell device performance.<sup>67</sup> High power efficiency might be achieved by a solar cell with a long diffusion length and low binding energy. Hybrids have a lower exciton binding energy than organic materials, as is widely known. This is because their dielectric constants differ.<sup>68</sup> It is obvious that the dielectric constant is a critical element in determining the binding energy for photocurrent generation in solar cells.<sup>68</sup> As a result of the C<sub>6</sub>H<sub>9</sub>N<sub>2</sub>FeCl<sub>4</sub> high dielectric constant, it might be employed as a dielectric gate or active channel in FET devices.<sup>69,70</sup> The FET, a common component in current electronic circuits, is used to amplify or tune electronic analog and digital signals.

The complex dielectric data collected at various temperatures were adjusted using the Cole-Cole equation to study temperature-dependent dipolar polarisation and associated relaxation processes.

The Cole-Cole formula is given by:<sup>71</sup>

$$\epsilon = \epsilon_{\infty} + \frac{\epsilon_s - \epsilon_{\infty}}{1 + (i\omega\tau)^{1-\alpha}} \quad (10)$$

The real and imaginary components of are provided by:<sup>72</sup>

$$\epsilon' = \epsilon_{\infty} + \frac{(\epsilon_s - \epsilon_{\infty}) \left[ 1 + (\omega\tau)^m \cos\left(\frac{m\pi}{2}\right) \right]}{1 + 2(\omega\tau)^m \cos\left(\frac{m\pi}{2}\right) + (\omega\tau)^{2m}} \quad (11)$$

$$\epsilon'' = \epsilon_{\infty} + \frac{(\epsilon_s - \epsilon_{\infty})(\omega\tau)^m \sin\left(\frac{m\pi}{2}\right)}{1 + 2(\omega\tau)^m \cos\left(\frac{m\pi}{2}\right) + (\omega\tau)^{2m}} \quad (12)$$

where  $\omega$  is the angular frequency,  $\tau$  is the relaxation time, and  $\alpha$  is a material-dependent constant related to the width of the distribution of relaxation times ( $m = 1 - \alpha$ ).<sup>73</sup> Furthermore, in the low and high frequency limits, respectively,  $\epsilon_s$  and  $\epsilon_{\infty}$  are the dielectric constants.

Eqn (11) was used to fit the actual component of the obtained dielectric constant *versus* frequency data (Fig. 11) to get different dielectric and relaxation characteristics of the C<sub>6</sub>H<sub>9</sub>N<sub>2</sub>FeCl<sub>4</sub> sample. All of the parameters acquired from the fits are presented in Fig. 12 it is observed that  $\epsilon_s$  and  $\epsilon_{\infty}$  values are nearly temperature independent. A slight increase in the values of  $\epsilon_s$  and  $\epsilon_{\infty}$  when temperatures rise over 333 K can be attributed to the contribution of thermally produced charge carriers. Furthermore, as predicted, when the measurement temperature rises, the mean relaxation time ( $\tau$ ) decreases.



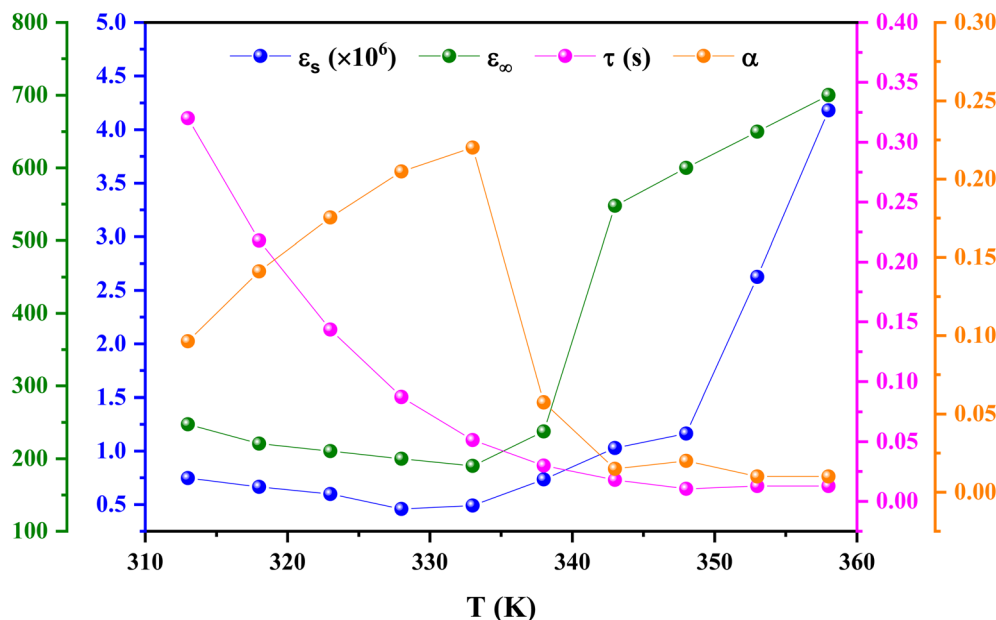


Fig. 12 Temperature dependency of the extracted fitting parameters for 2A5PFeCl<sub>4</sub>.

The parameter  $\alpha$  provides information about the sample's relaxation time distribution. It's worth noting that begins to rise from 0.09 at 313 K to a high of 0.22 at 333 K before falling to 0.009 at 358 K. This fluctuation demonstrates that as the temperature rises, other relaxation mechanisms with varying relaxation times begin to participate, resulting in a wide range of relaxation times with a maximum value at 333 K. Above 333 K, the relaxation time distribution narrows. The relaxation of the dipoles in grains and grain boundaries appears to approach identical relaxation times as the temperature rises, and both distributions progressively overlap, resulting in a small relaxation time breadth at high temperatures. In contrast, when the temperature drops below 358 K, the difference between the distribution of relaxation times owing to dipoles at the grains and grain boundary regions appears, resulting in a broader variety of relaxation times at 333 K. A further decrease in temperature freezes the grain boundary relaxation processes, resulting in a narrowing of the relaxation time distribution (*i.e.*, a drop in the value of  $\alpha$ ).<sup>74</sup>

On the contrary, it was absolutely crucial to study in the materials for applications in optoelectronics the “dissipation factor” which is represented by  $\tan(\delta)$  in Fig. 13, where  $\delta$  is mathematically defined as the angle between the voltage and charging current, also known as “loss angle”.<sup>75</sup> The dielectric loss was mainly due to different physical phenomena, such as the conduction process, the dielectric relaxation, the molecular dipole moment, and the interfacial polarization.<sup>76</sup>

In the low frequency range, more energy is required to produce charge carrier movement. As a result,  $\tan(\delta)$  values are higher in this frequency range.<sup>77</sup> The resistivity of the material reduces with increasing frequency, so the movement of charge carriers consumes less energy. As a result, the dielectric loss in the high frequency area decreases. This paved the way for these materials to be considered for use in electrical devices.<sup>78</sup>

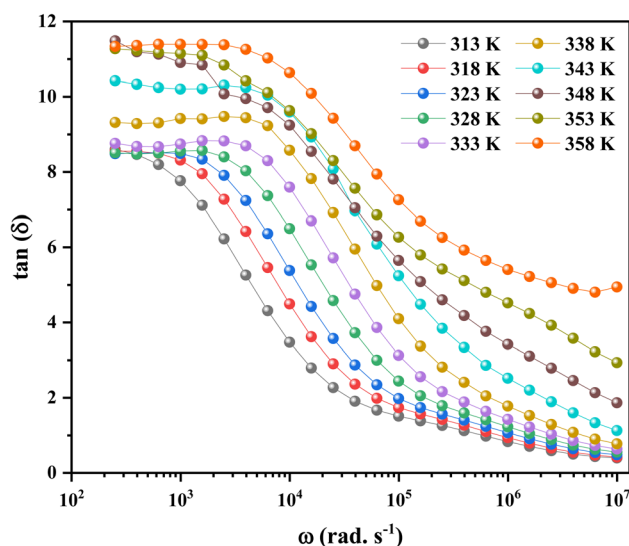


Fig. 13 Frequency-dependent dielectric loss of 2A5PFeCl<sub>4</sub>.

It also shows that higher temperatures and lower frequencies result in more dielectric loss, which exhibits a clear sign of the growth in the conductivity of the material.<sup>79</sup>

The complex polarizability  $\alpha$ , put out by Scaife,<sup>80</sup> was the subject of attention in order to better comprehend the processes of dielectric relaxation. This makes it possible to investigate a compound's inherent dielectric characteristics more thoroughly since it gives each polarisation process the attention it deserves. In fact, different coexisting relaxation processes in a sample might be easily distinguished by employing this formalism. As a result, the complex polarizability is described as:





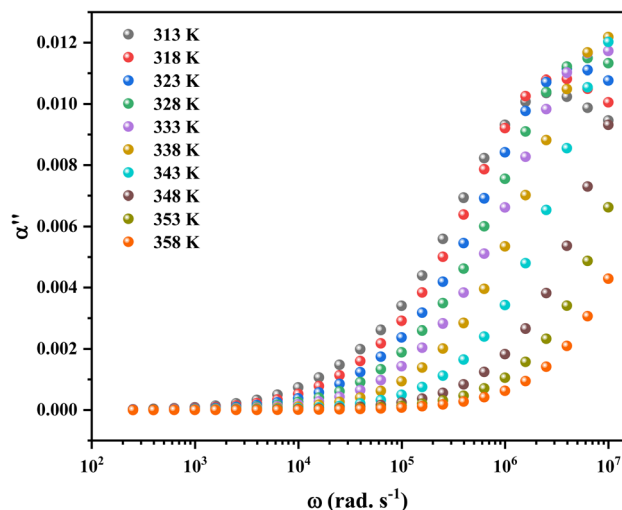


Fig. 14 The imaginary part of complex polarizability as a function of frequency.

$$\alpha = \alpha' - i\alpha'' = \frac{\varepsilon + 1}{\varepsilon + 2} \quad (13)$$

where the real and imaginary components of the complex polarizability, respectively, are  $\alpha'$  and  $\alpha''$  and  $\varepsilon$  is the complex dielectric constant. It is possible to determine the imaginary part of the complex polarizability parameter  $\alpha''$  using the relation given below:<sup>81</sup>

$$\alpha'' = \frac{2\varepsilon''}{(\varepsilon' + 2)^2 + \varepsilon''^2} \quad (14)$$

Fig. 14 shows the imaginary part of the complex polarizability as a function of frequency and temperature. As the temperature rises, this displays relaxation peaks with a maximum frequency  $\omega_{zM}$  that shift toward a high frequency (see Fig. S2†). This variation displays the Arrhenius behaviour:

$$\omega_{zM} = \omega_{z0} \exp\left(-\frac{E_a}{k_B T}\right) \quad (15)$$

where  $\omega_{z0}$  is a pre-factor,  $T$  is the temperature,  $k$  is the Boltzmann constant and  $E_a$  is the activation energy, which is  $E_{a1} = 0.85$  eV in the range [313–333 K] and  $E_{a2} = 1.65$  eV in the range [343–358 K].

The study of electrical modulus provides insight into the electrode effect, grain boundary effect, grain characteristics, conductivity, and relaxation behaviour of the material. This technique is also useful to understand its transport process and relaxation mechanism.

The complex electric modulus is represented by the equation:  $M = M' + iM''$ . The following formula<sup>82</sup> has been used to determine  $M'$ :

$$M' = \frac{\varepsilon'}{\varepsilon'^2 + \varepsilon''^2} \quad (16)$$

Fig. 15a depicts the frequency dependence of the real components of the modulus spectra ( $M'(T, f)$ ) between 313 and 358 K. At all temperatures, the value of  $M'$  increases as frequency increases. At low frequencies,  $M'$  approaches 0, proving that there is no electrode influence. The  $M'$  value falls in this region (low frequency) and gradually rises with increasing frequency because the electric field formed is insufficient to provide the necessary restoring force for the movement of the charge carriers. As a result, the conduction process is brought on by the short-range mobility of charge carriers.<sup>83</sup>

The same formula has been used to estimate  $M''$ :

$$M'' = \frac{\varepsilon''}{\varepsilon'^2 + \varepsilon''^2} \quad (17)$$

Fig. 15b shows the curve of  $M''$  with frequency at various temperatures. The value of  $M''$  rose steadily as frequency increased, peaked ( $M''_{\max}$ ), and then rapidly fell, as shown in this chart. The peak shifting toward a higher frequency with rising temperature indicates the presence of the relaxation process. A change in capacitance is shown by the variation in  $M''_{\max}$  value with temperature. The asymmetrical broadening of the peak, which denotes non-Debye type conduction events, indicates the transmission of relaxation in the material.<sup>84</sup>

Following the expression in eqn (18) below, which applies the complex electric modulus Laplace transformation, we performed the analysis of the  $M''$  data's frequency dependency, which is shown below:

$$M = M_{\infty} \left[ 1 - \int_0^{\infty} e^{-ift} \left( \frac{d\phi}{dt} \right) dt \right] \quad (18)$$

The relaxation function  $\phi(t)$  provides details on the temporal evolution of the electric field ( $E$ ) within the compound,<sup>85</sup> while  $M_{\infty} (=1/\varepsilon_{\infty})$  in the preceding formula reflects the inverse of the real component  $\varepsilon_{\infty}$  of the dielectric permittivity's high frequency asymptotic value.

It is clear that the asymmetrical plots in Fig. 15b offer indications of the non-exponential behavior of the electrical modulus characterized by a non-exponential decay function and the Kohlrausch–Williams–Watts (KWW) parameter, which is written as:<sup>86,87</sup>

$$\phi(t) = \exp \left[ -\left( \frac{t}{\tau_0} \right)^{\beta} \right] \quad (19)$$

With an increase in the relaxation time distribution, the stretched exponential parameter normally decreases.<sup>88</sup> The above expression's variable, which describes the degree of linearity deviation,  $\beta$  is in the range  $0 < \beta < 1$ . As the system approaches unity ( $\beta \rightarrow 1$ ), Debye relaxation is visible. On the other hand,  $\beta \rightarrow 0$  refers the amount of ion contact that takes place in the system. In accordance with Bergman's modified analysis of the KWW function, we applied the mathematical fitting method to enable direct evaluation of modulus plots in the frequency domain as shown:<sup>88</sup>





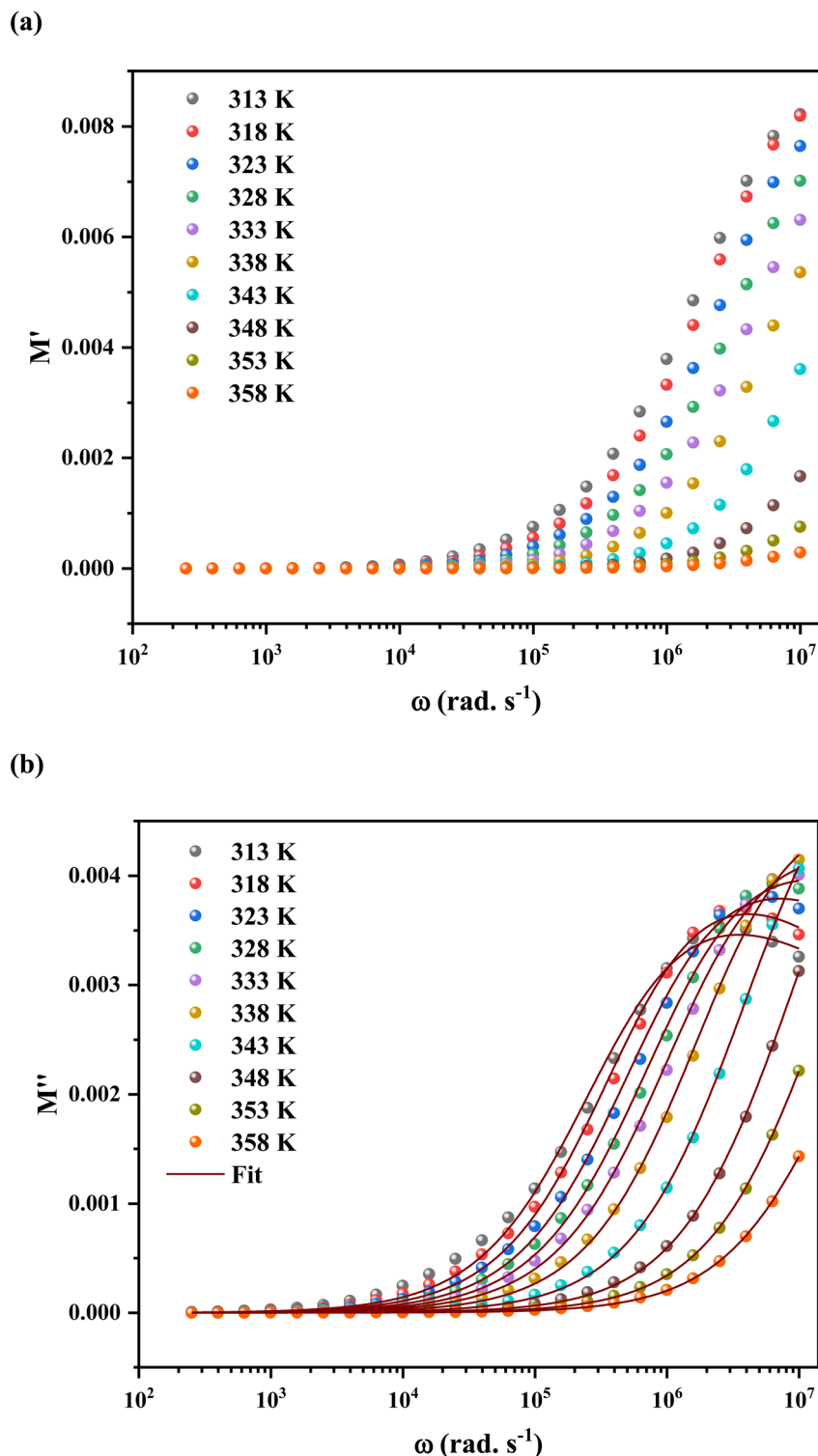


Fig. 15 Frequency dependent of (a)  $M'$  and  $M''$  (b) at different temperatures of 2A5PF<sub>6</sub>Cl<sub>4</sub>.

$$M''(f) = \frac{M''_{\max}}{\left[ (1 - \beta) + \left( \frac{\beta}{1 + \beta} \right) \left[ \beta \left( \frac{\omega_{\max}}{\omega} \right) + \left( \frac{\omega_{\max}}{\omega} \right)^{\beta} \right] \right]} \quad (20)$$

Here,  $M''_{\max}$  is the imaginary portion of the  $M$  peak value with a matching frequency of  $\omega_{\max}$ . The red solid lines in Fig. 15b

represents the nonlinear fitting of the aforementioned formula to the empirically determined modulus values for the system under inquiry. The corresponding parameters extrapolated from the fitting are shown in Table 6. The values of  $\beta$  range from 0.65 to 0.92, indicating that non-Debye type relaxation processes predominate in this system.



**Table 6** The list of parameters obtained by fitting the modified KWW function (eqn (8)) to the frequency dependent modulus ( $M''$ ) data

$T$ (K)	$M''_{\max}$ ( $\times 10^{-3}$ )	$\beta$	$\omega_{\max}$ ( $\times 10^6$ )	$\tau_0$ ( $\times 10^{-6}$ )
313	3.46	0.293	3.509	1.789
318	3.65	0.325	4.133	1.519
323	3.79	0.291	7.107	0.883
328	3.96	0.261	12.19	0.514
333	4.13	0.246	19.38	0.323
338	4.42	0.255	30.33	0.207
343	5.59	0.065	942.6	$6.662 \times 10^{-3}$
348	5.85	0.043	4802	$1.307 \times 10^{-3}$
353	5.6	0.041	9220	$6.811 \times 10^{-4}$
358	4.33	0.039	13 330	$4.708 \times 10^{-4}$

In order to better understand material properties and their importance in optoelectronic devices, as well as to learn more about the nature of the transport mechanism and to comprehend how charge carriers interact, the electrical conductivity behavior was examined.<sup>89</sup> The following law was used by Jonscher's to try and explain how ac conductivity behaves.<sup>90</sup>

$$\sigma_{ac}(\omega) = \sigma(0) + \sigma_1(\omega) = \sigma_{dc} + A\omega^s \quad (21)$$

where  $\sigma_{ac}(\omega)$  is the total measured conductivity,  $\sigma(0) = \sigma_{dc}$  is the frequency independent term giving the conductivity in continuous current,  $\sigma_1(\omega)$  is the pure dispersive component of ac conductivity having a characteristic of power law in the angular frequency  $\omega$  domain with an exponent  $s$ . The value of  $s$  is in the range of  $0 < s < 1$  and is frequency independent but temperature and material dependent.  $A$  is a constant for a particular temperature.

The ac conductivity *versus* frequency plots (usually referred to as conductivity spectra) for 2A5PFeCl<sub>4</sub> at various temperatures are presented in Fig. 16. Free as well as bound carriers can cause frequency dependence in ac conductivity. If the

conduction is caused by free carriers, then the  $\sigma_{ac}$  must decrease as the frequency rises.<sup>91</sup> Because the measured ac conductivity decreased when the frequency was reduced in our example, the observed ac conductivity must be related to the bound carriers trapped in the sample. The Schottky barrier at the metal-dielectric interface, Maxwell-Wagner type conduction, and hopping conduction<sup>91</sup> can all be used to explain the phenomenon of increased conductivity with increasing frequency. The disordering of cations between neighboring sites, *i.e.*, neighboring grains and their boundaries, as well as the presence of space charges, may explain the positive slope of ac conductivity with frequency.

A closer look at the conductivity plots reveals that the curves show high-frequency dispersion that follows Jonscher's power law equation (eqn (21)). According to Jonscher, the relaxation processes caused by mobile charge carriers are the source of conductivity's frequency dependency. A mobile charge remains in a condition of displacement between two potential energy minima when it jumps to a new site from its original location.<sup>92</sup>

In addition, the material conduction behavior follows a power law,  $\sigma_{ac} \propto \omega^s$ , with a slope shift governed by  $s$ . The parameter  $s$  describes the interaction between the charge carriers involved in the polarization process. The interaction, on the other hand, increases as the temperature rises, resulting in a drop in  $s$  from 0.62 to 0.30 (right of Fig. 17), suggesting the correlated barrier hopping (CBH) conduction mechanism. In addition, these numbers imply that the system is far from being in a Debye type state ( $s = 1$ ).<sup>93</sup> However, at 313 K, the dc conductivity of the C<sub>6</sub>H<sub>9</sub>N<sub>2</sub>FeCl<sub>4</sub> was in the order of  $10^{-4}$  S cm<sup>-1</sup>, which was comparable to the perovskites C<sub>3</sub>H<sub>7</sub>NH<sub>3</sub>PbI<sub>3</sub>.<sup>94</sup> As a consequence, the high dielectric permittivity and electrical conductivity evaluations resulted in better conducting capabilities, indicating that this material might be used in FET devices.

The data of dc conductivity is displayed as  $\ln(\sigma_{dc})$  vs.  $1000/T$  at the temperature range of 313–358 K (left of Fig. 17), revealing Arrhenius type behavior as indicated by:

$$\sigma_{dc} = \sigma_0 \exp\left(-\frac{E_a}{k_B T}\right) \quad (22)$$

where  $\sigma_0$  is the pre-exponential factor,  $k_B$  is the Boltzmann constant, and  $E_a$  is the activation energy.

The dc conductivity increases as the temperature rises. In addition, we can see two regions associated with two activation energies,  $E_{a1} = 0.58$  eV in the range [313–333 K] and  $E_{a2} = 1.23$  eV in the range [343–358 K]. On the other hand, the deduced activation energies from the ac conductivity as a function of reciprocal temperature for five fixed frequencies (Fig. 18) are listed in Table 7. It's worth noting that when the frequency rises, the activation energies of both temperature areas drop. This supports the idea that increasing the applied field frequency enhances the electrical hops between localized states. Furthermore, the ac conduction activation energies at high frequencies are shown to be smaller than those at low frequencies. This is due to the fact that at high frequencies, the conductivity is taken up by the mobility of charge carriers over

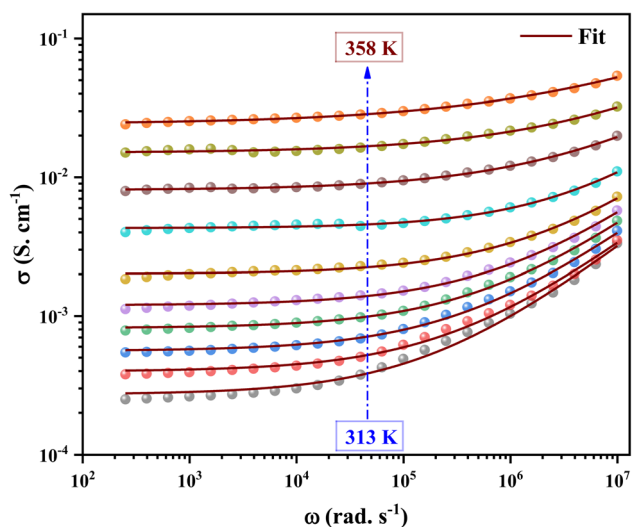


**Fig. 16** The variation of the electrical conductivity *versus* the frequency at different temperatures.



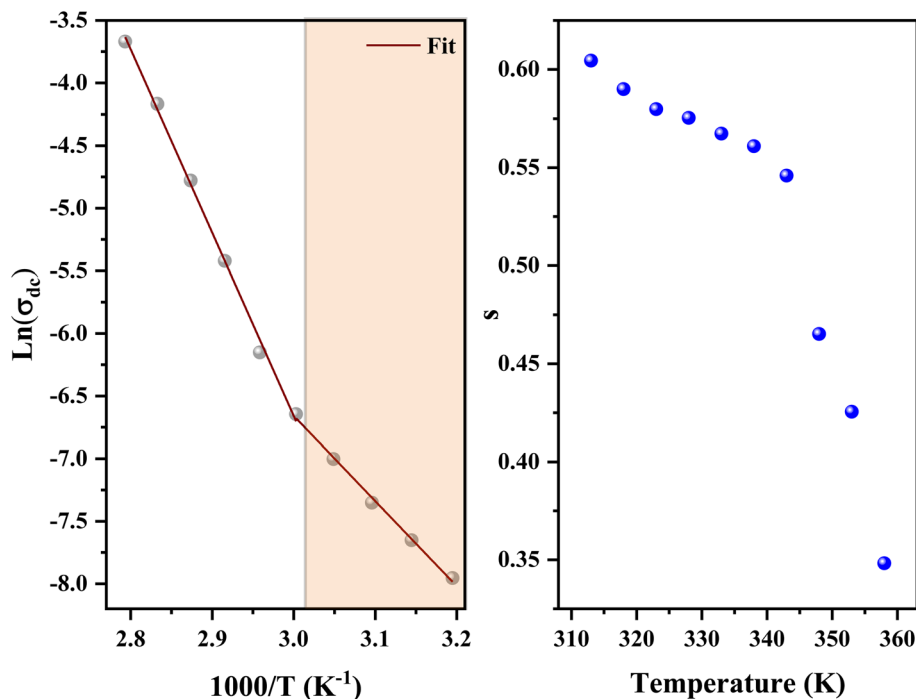


Fig. 17 Variation of  $\ln(\sigma_{dc})$  vs.  $(1000/T)$  (left) and the variation of the exponents as a function of temperature (right).

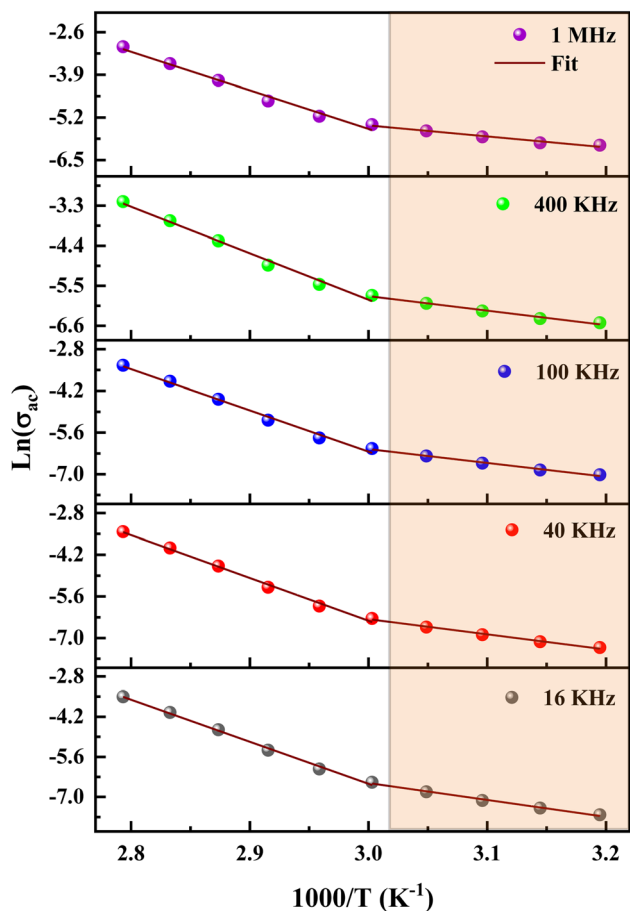


Fig. 18 Variation of  $\ln(\sigma_{ac})$  as a function of temperature at different frequencies.

short distances and needs less energy than the one necessary for mobility over longer distances at low frequencies.<sup>56</sup>

To conclude the study of the dielectric properties of the studied compound, capacitance measurements were done at the same frequencies and temperatures. The behavior of capacitance as the angular frequency increases from  $10^2$  to  $10^7$  rad s<sup>-1</sup> at temperatures ranging from 313 to 358 K is shown in Fig. 19. It can be clearly seen that the capacitance curve decreases with increasing frequency, and the maximum values are found at low frequencies. This capacitive characteristic indicates an inhomogeneous barrier formation at the interface due to the presence of interface states. These states can result in the creation of an interfacial space charge at the interface.<sup>95,96</sup> The contribution of the ionic capacitance decreased with the drop in temperature. However, at high frequencies, the capacitance became saturated and plateaued. This was attributed to the contribution of the external circuit's resistance in series, as well as the geometric capacitance of the pellet, which was related to the permittivity as shown in eqn (23):<sup>97</sup>

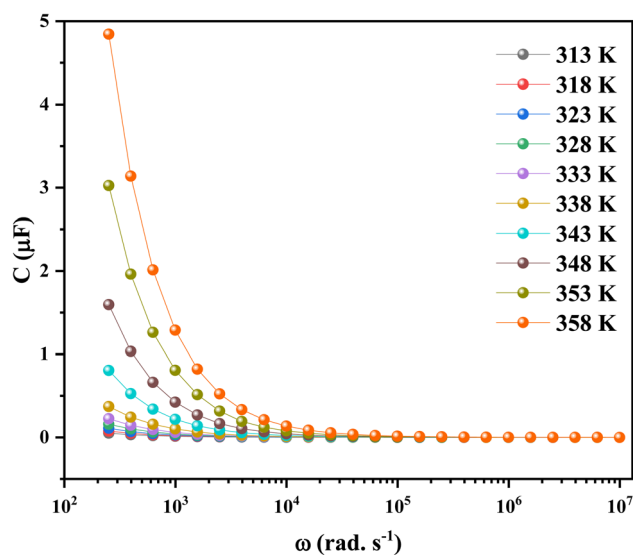
$$C = \frac{\epsilon A}{d} \quad (23)$$

where  $A$  refers to the area of the electrode and  $d$  shows the pellet thickness. According to eqn (23), the capacitance depends on the dielectric permittivity. As previously found in permittivity measurements, the capacitance of materials fell and became steady. In addition, the capacitance values of the material calculated at 313 were in the order of  $10^{-6}$  F. So, a high capacitance could generally enhance the performance of FET devices.



Table 7 Activation energies obtained for selected frequencies

$f$	$E_{a1}$ (eV)	$E_{a2}$ (eV)
16 kHz	0.5	1.22
40 kHz	0.44	1.20
100 kHz	0.4	1.16
400 kHz	0.34	1.06
1 MHz	0.28	0.99

Fig. 19 Frequency dependence of capacitance spectra of 2A5PFeCl<sub>4</sub>.

## 5. Conclusion

In summary, the 2A5PFeCl<sub>4</sub> compound was successfully prepared through the slow evaporation solution growth method at room temperature, and its structural, optical, and extensive dielectric properties are investigated. The structural geometry was optimized using the DFT/B3LYP-D3 method. The structural parameters are in good agreement with the experimental data. The absorption spectra have been recorded and simulated at the TD/B3LYP-D3/lanl2dz level of theory. As a result, there is good agreement between theoretical absorption and experimental spectra.

UV-vis spectral analysis allows for the exploration of the optical characteristics of the title compound and the determination of a band gap energy of 2.47 eV. Hirshfeld surface analysis demonstrated that hydrogen bonding interactions are primarily responsible for the structure packing's stabilization. The AIM and NCI-RDG topological analyses prove that the interactions between the organic and inorganic parts are mainly of the van der Waals type. The MEP surface ascertains the donor-acceptor interactions within the title compound, showing the electrophilic and nucleophilic sites.

The huge dielectric permittivity, strong capacitance, high conductivity, and low dielectric loss of this material make it highly tunable for FET applications as compared to other dielectric materials. They might be used as semiconductors,

dielectric gates, or active channels in novel transistor devices due to their better dielectric properties. The findings of our research help to explain why the C<sub>6</sub>H<sub>9</sub>N<sub>2</sub>FeCl<sub>4</sub> has such good dielectric properties. More specifically, our research outlined the benefits as well as the efficacy of these materials in FET applications. However, knowing the underlying electrical characteristics of these materials is required for future views on developing and achieving low-cost and high-performance FET devices based on them.

## Conflicts of interest

The authors declare no competing interests.

## References

- 1 M. Mas-Torrent and C. Rovira, *Chem. Rev.*, 2011, **111**, 4833–4856.
- 2 J. Park, H. H. Nguyen, A. Woubit and M. Kim, *Appl. Sci. Convergence Technol.*, 2014, **23**, 61–71.
- 3 J. Y. Tsao, S. Chowdhury, M. A. Hollis, D. Jena, N. M. Johnson, K. A. Jones and J. A. Simmons, *Adv. Electron. Mater.*, 2018, **4**, 1600501.
- 4 B. Crone, A. Dodabalapur, Y. Y. Lin, R. W. Filas, Z. Bao, A. La Duca and W. Li, *Nature*, 2000, **403**, 521–523.
- 5 R. P. Ortiz, A. Facchetti and T. J. Marks, *Chem. Rev.*, 2010, **110**, 205–239.
- 6 A. I. Kingon, J. P. Maria and S. K. Streiffer, *Nature*, 2000, **406**, 1032–1038.
- 7 J. M. Ramirez, H. Elfaiki, T. Verolet, C. Besancon, A. Gallet, D. Néel and M. Achouche, *IEEE J. Sel. Top. Quantum Electron.*, 2019, **26**, 1–13.
- 8 S. P. Senanayak, M. Abdi-Jalebi, V. S. Kamboj, R. Carey, R. Shivanna, T. Tian and H. Sirringhaus, *Sci. Adv.*, 2020, **6**, eaaz4948.
- 9 S. Hajlaoui, I. Chaabane, A. Oueslati, K. Guidara and A. Bulou, *Spectrochim. Acta, Part A*, 2014, **117**, 225–233.
- 10 B. Yan, J. W. Wang and Y. J. Li, *J. Alloys Compd.*, 2011, **509**, 9240–9245.
- 11 L. H. Oliveira, A. P. de Moura, E. Longo, J. A. Varela and I. L. Rosa, *J. Alloys Compd.*, 2013, **579**, 227–235.
- 12 C. Ji, P. Wang, Z. Wu, Z. Sun, L. Li, J. Zhang, W. Hu, M. Hong and J. Luo, *Adv. Funct. Mater.*, 2018, **28**, 1705467.
- 13 Q. Zhang, S. T. Ha, X. Liu, T. C. Sum and Q. Xiong, *Nano Lett.*, 2014, **14**, 5995–6001.
- 14 C. Geffroy, E. Grana, T. Bessho, S. Almosni, Z. Tang, A. Sharma, T. Kinoshita, F. Awai, E. Cloutet, T. Toupance, H. Segawa and G. Hadzioannou, *ACS Appl. Energy Mater.*, 2020, **3**, 1393–1401.
- 15 H. Wensi Cai, *Sci. Bull.*, 2021, **66**, 648.
- 16 N. D. Canicoba, N. Zagni, F. Liu, G. Mccuistian, K. Fernando, H. Bellezza and A. D. Mohite, *ACS Mater. Lett.*, 2019, **1**, 633–640.
- 17 E. J. Juarez-Perez, R. S. Sanchez, L. Badia, G. Garcia-Belmonte, Y. S. Kang, I. Mora-Sero and J. Bisquert, *J. Phys. Chem. Lett.*, 2014, **5**, 2390.



- 18 C. R. Kagan, D. B. Mitzi and C. D. Dimitrakopoulos, *Science*, 1999, **286**, 945.
- 19 M. Tahenti, S. Gatfaoui, N. Issaoui, T. Roisnel and H. Marouani, *J. Mol. Struct.*, 2020, **1207**, 127781.
- 20 A. Oueslati, A. Bulou, F. Calvayrac, K. Adil, M. Gargouri and F. Hlel, *Vib. Spectrosc.*, 2013, **64**, 10–20.
- 21 M. Hamdi, S. Karoui, A. Oueslati, S. Kamoun and F. Hlel, *J. Mol. Struct.*, 2018, **1154**, 516–523.
- 22 L. J. Farrugia, *J. Appl. Crystallogr.*, 2012, **45**, 849e854.
- 23 K. Brandenburg and H. Putz, *DIAMOND Crystal Impact GbR*, Bonn, Germany, 1999.
- 24 M. J. Frisch, W. Trucks, G. H. B. Schlegel, G. E. Scuseria, M. A. Robb and J. R. G. Cheeseman, *GAUSSIAN*, 2009.
- 25 R. I. Dennington, T. Keith and J. Millam, *GaussView, Version 5.0.8*, Semichem. Inc., Shawnee Mission, KS, 2008.
- 26 A. D. Becke, *J. Chem. Phys.*, 1996, **104**, 1040–1046.
- 27 C. Lee, W. Yang and R. G. Parr, *Phys. Rev. B: Condens. Matter Mater. Phys.*, 1988, **37**, 785.
- 28 S. Grimme, J. Antony, S. Ehrlich and H. Krieg, *J. Chem. Phys.*, 2010, **132**, 154104.
- 29 P. J. Hay and W. R. Wadt, *J. Chem. Phys.*, 1985, **82**, 299.
- 30 M. A. Spackman and D. Jayatilaka, *Cryst. Eng. Comm.*, 2009, **11**, 19–32.
- 31 H. Wang, H. Xiao, N. Liu, B. Zhang and Q. Shi, *Open J. Inorg. Chem*, 2015, **5**, 63.
- 32 T. Lu and F. Chen, *J. Comput. Chem.*, 2012, **33**, 580–592.
- 33 I. B. Gharbia, R. Kefi, C. B. Nasr and A. Durif, *Rev. Roum. Chim.*, 2008, **53**, 169–175.
- 34 L. Yang, D. R. Powell and R. P. Houser, *Dalton Trans*, 2007, **9**, 955–964.
- 35 W. H. Baur, *Acta. Crystallogr., B: Struct. Sci., Cryst. Eng. Mater.*, 1974, **30**, 1195–1215.
- 36 R. Elweij and F. Hlel, *Phys. E*, 2016, **84**, 498–504.
- 37 N. A. Dlala, Y. Bouazizi, H. Ghalla and N. Hamdi, *J. Chem.*, 2021, **12**, 1–17.
- 38 R. F. Bader, *Atoms in Molecules a, Quantum Theory (AIM)*, 1990.
- 39 T. B. Issa, F. Sayari, H. Ghalla and L. Benhamada, *J. Mol. Struct.*, 2019, **1178**, 436–449.
- 40 P. L. A. Popelier and R. F. W. Bader, *Chem. Phys. Lett.*, 1992, **189**, 542–548.
- 41 X. Niu, Z. Huang, L. Ma, T. Shen and L. Guo, *Chem. Sci. J.*, 2013, **125**, 949–958.
- 42 F. J. Luque, J. M. López and M. Orozco, *Theor. Chem. Acc.*, 2000, **103**, 343–345.
- 43 N. Okulik and A. H. Jubert, *Internet Electron. J. Mol. Des.*, 2005, **4**, 17–30.
- 44 K. Y. Shi, L. L. Guo, H. X. Liu, L. Zou and S. F. Ying, *Solid State Phenom.*, 2006, **111**, 119–122.
- 45 C. Zhou, X. Yu, H. Ma, X. Huang, H. Zhang and J. Jin, *Carbohydr. Polym.*, 2014, **105**, 300–307.
- 46 H. L. Friedman, *J. Am. Chem. Soc.*, 1952, **74**, 5–10.
- 47 T. Backer, O. Breunig, M. Valldor, K. Merz, V. Vasylyeva and A. V. Mudring, *Cryst. Growth Des.*, 2011, **11**, 2564–2571.
- 48 R. E. Marotti, D. N. Guerra, C. Bello, G. Machado and E. A. Dalchiele, *Sol. Energy Mater. Sol. Cells*, 2004, **82**, 85–103.
- 49 R. Henriquez, P. Grez, E. Munoz, H. Gomez, J. A. Badan, R. E. Marotti and E. A. Dalchiele, *Thin Solid Films*, 2010, **518**, 1774–1778.
- 50 P. Kubelka and F. Munk, *Z. Phys.*, 1931, **12**, 593–601.
- 51 I. B. Saad, N. Hannachi, T. Roisnel and F. Hlel, *J. Adv. Dielectr.*, 2019, **9**, 1950040.
- 52 M. Belletête, J. F. Morin, M. Leclerc and G. Durocher, *J. Phys. Chem.*, 2005, **109**, 6953–6959.
- 53 N. Mhadhbi, S. Saïd, S. Elleuch and H. Naïli, *J. Mol. Struct.*, 2016, **1108**, 223–234.
- 54 S. Y. Ebrahimipour, M. Khosravan, J. White and S. Fekri, *Appl. Organomet. Chem.*, 2018, **32**, e4233.
- 55 Y. Dang, C. Zhong, G. Zhang, D. Ju, L. Wang, S. Xia and X. Tao, *Chem. Mater.*, 2016, **28**, 6968–6974.
- 56 W. B. Weir, *Proc. IEEE*, 1974, **62**, 33–36.
- 57 T. Dabbebi, S. Hcini, B. Alzahrani, H. Rahmouni, E. Dhahri, H. AlRobei and M. L. Bouazizi, *J. Mater. Sci.: Mater. Electron.*, 2022, **33**, 490–504.
- 58 F. Hcini, S. Hcini, B. Alzahrani, S. Zemni and M. L. Bouazizi, *Appl. Phys. A*, 2020, **126**, 362.
- 59 A. Sahoo, T. Paul, S. Maiti and R. Banerjee, *Nanotechnology*, 2022, **33**, 195703.
- 60 K. W. Wagner, *Ann. Phys.*, 1913, **4**, 817.
- 61 S. Kumari, N. Ortega, A. Kumar, S. P. Pavunny, J. W. Hubbard, C. Rinaldi and R. S. Katiyar, *J. Appl. Phys.*, 2015, **117**, 114102.
- 62 S. Patra, P. Sengupta, A. Ray, A. Roy and S. Das, *Ceram. Int.*, 2018, **44**, 14236–14241.
- 63 G. A. Samara, *Phys. Rev. B: Condens. Matter Mater. Phys.*, 1983, **27**, 3494.
- 64 Q. Li, R. Cao, J. Cho and G. Wu, *Adv. Energy Mater.*, 2014, **4**, 1301415.
- 65 Z. Fu, X. Zhang, H. Zhang, Y. Li, H. Zhou and Y. Zhang, *Chin. J. Chem.*, 2021, **39**, 381.
- 66 J. Gao, Y. Wang, Y. Liu, X. Hu, X. Ke, L. Zhong and X. Ren, *Sci. Rep.*, 2017, **7**, 1.
- 67 M. Ahmadi, T. Wu and B. Hu, *Adv. Mater.*, 2017, **29**, 1605242.
- 68 Y. C. Hsiao, T. Wu, M. Li, Q. Liu and W. B. Hu, *J. Mater. Chem. A*, 2015, **3**, 15372.
- 69 A. Daus, C. Roldan-Carmona, K. Domanski, S. Knobelspies, G. Cantarella, C. Vogt and G. Troster, *Adv. Mater.*, 2018, **30**, 1707412.
- 70 C. R. Kagan, D. B. Mitzi and C. D. Dimitrakopoulos, *Science*, 1999, **286**, 945.
- 71 K. S. Cole and R. H. Cole, *J. Chem. Phys.*, 1941, **9**, 341–351.
- 72 A. Ghoudi, K. B. Brahim, A. Oueslati, K. Khirouni and A. Aydi, *J. Mater. Sci.: Mater. Electron.*, 2022, 1–15.
- 73 D. Ming, J. M. Reau, J. Ravez, J. Gitae and P. Hagenmuller, *J. Solid State Chem.*, 1994, **116**, 185–192.
- 74 V. Khopkar and B. Sahoo, *Phys. Chem. Chem. Phys.*, 2020, **22**, 2986–2998.
- 75 P. Bhuyan, D. Cho, M. Choe, S. Lee and S. Park, *Polymers*, 2022, **14**, 710.
- 76 K. C. Kao, *Dielectric Phenomena in Solids*, Elsevier, Amsterdam, 2004.





- 77 F. Gaâbel, M. Khelifi, N. Hamdaoui, L. Beji, K. Taïbi and J. Dhahri, *J. Mater. Sci.: Mater. Electron.*, 2019, **30**, 14823–14833.
- 78 S. Singh, G. Banappanavar and D. Kabra, *ACS Mater. Lett.*, 2020, **5**, 728.
- 79 W. Wan, J. Luo, C.-e. Huang, J. Yang, Y. Feng, W.-X. Yuan, Y. Ouyang, D. Chen and T. Qiu, *Ceram. Int.*, 2018, **44**, 5086–5092.
- 80 B. K. P. Scaife, *Proc. Phys. Soc.*, 1963, **81**, 124.
- 81 I. B. Slima, K. Karoui, A. Mahmoud, F. Boschini and A. B. Rhaïem, *RSC Adv.*, 2022, **12**, 1563–1570.
- 82 C. Rayssi, S. E. Kossi, J. Dhahri and K. Khirouni, *RSC Adv.*, 2018, **8**, 17139–17150.
- 83 R. Das and R. N. P. Choudhary, *Solid State Sci.*, 2019, **87**, 1–8.
- 84 R. Ranjan, R. Kumar, N. Kumar, B. Behera and R. N. P. Choudhury, *J. Alloy. Comp.*, 2011, **509**, 6388.
- 85 I. M. Hodge and C. A. Angell, *J. Chem. Phys.*, 1977, **67**, 1647–1658.
- 86 K. L. Ngai, *J. Non-Cryst. Solids*, 1996, **203**, 232–245.
- 87 J. Hazarika and A. Kumar, *Synth. Met.*, 2014, **198**, 239–247.
- 88 R. Bergman, *J. Appl. Phys.*, 2000, **88**, 1356–1365.
- 89 A. Starczewska, B. Toron, P. Szperlich and M. Nowak, *Materials*, 2021, **14**, 2579.
- 90 A. K. Jonscher, *Nature*, 1977, **276**, 673–679.
- 91 R. Thomas, V. K. Varadan, S. Komarneni and D. C. Dube, *J. Appl. Phys.*, 2001, **90**, 1480–1488.
- 92 P. R. Das, B. N. Parida, R. Padhee and R. N. P. Choudhary, *J. Adv. Ceram.*, 2013, **2**, 112–118.
- 93 W. K. Lee, J. F. Liu and A. S. Nowick, *Phys. Rev. Lett.*, 1991, **67**, 1559–1561.
- 94 P. Sengupta, P. Sadhukhan, A. Ray, R. Ray, S. Bhattacharyya and S. Das, *J. Appl. Phys.*, 2020, **127**, 204103.
- 95 G. R. Neupane, M. Bamidele, V. Yeddu, D. Y. Kim and P. Hari, *J. Mater. Res.*, 2022, **37**, 1357–1372.
- 96 H. H. Gullu and D. E. Yildiz, *J. Mater. Sci.: Mater. Electron.*, 2021, **32**, 13549–13567.
- 97 Y. Zheng, A. Fischer, N. Sergeeva, S. Reineke and S. C. Mannsfeld, *Org. Electron.*, 2019, **65**, 82.

